Interannual to Interdecadal variability of winter and summer southern African rainfall, and their teleconnections.

Dieppois, B. , Pohl, B. , Rouault, M. , New, M. , Lawler, D. and Keenlyside, N.

RESEARCH ARTICLE

Key Points:
- Three time scales of summer and winter southern African rainfall variability are identified
- Tropical/subtropical teleconnections are related to summer rainfall variability
- Winter rainfall variability is influenced by the midlatitude atmospheric dynamics

Supporting Information:
- Supporting Information S1

Correspondence to:
B. Dieppois,
bastien.dieppois@coventry.ac.uk

Interannual to interdecadal variability of winter and summer southern African rainfall, and their teleconnections

Bastien Dieppois[1,2,3], Benjamin Pohl[4], Mathieu Rouault[3,5], Mark New[2], Damian Lawler[1], and Noel Keenlyside[5,6]

[1]Centre for Agroecology, Water and Resilience, Coventry University, Coventry, UK, [2]African Climate and Development Initiative, University of Cape Town, Cape Town, Republic of South Africa, [3]Department of Oceanography, MARE Institute, University of Cape Town, Cape Town, Republic of South Africa, [4]Centre de Recherches de Climatologie, UMR 6282 Biogéosciences, CNRS/Université de Bourgogne, Dijon, France, [5]Nansen-Tutu Center for Marine Environmental Research, University of Cape Town, Cape Town, Republic of South Africa, [6]Geophysical Institute, University of Bergen and Bjerknes Centre for Climate Research, Bergen, Norway

Abstract This study examines for the first time the changing characteristics of summer and winter southern African rainfall and their teleconnections with large-scale climate through the dominant time scales of variability. As determined by wavelet analysis, the austral summer and winter rainfall indices exhibit three significant time scales of variability over the twentieth century: interdecadal (15–28 years), quasi-decadal (8–13 years), and interannual (2–8 years). Teleconnections with global sea surface temperature and atmospheric circulation anomalies are established here but are different for each time scale. Tropical/subtropical teleconnections emerge as the main driver of austral summer rainfall variability. Thus, shifts in the Walker circulation are linked to the El Niño–Southern Oscillation (ENSO) and, at decadal time scales, to decadal ENSO-like patterns related to the Pacific Decadal Oscillation and the Interdecadal Pacific Oscillation. These global changes in the upper zonal circulation interact with asymmetric ocean-atmospheric conditions between the South Atlantic and South Indian Oceans; together, these lead to a shift in the South Indian Convergence Zone and a modulation of the development of convective rain-bearing systems over southern Africa in summer. Such regional changes, embedded in quasi-annular geopotential patterns, consist of easterly moisture fluxes from the South Indian High, which dominate southerly moisture fluxes from the South Atlantic High. Austral winter rainfall variability is more influenced by midlatitude atmospheric variability, in particular the Southern Annular Mode. The rainfall changes in the southwestern regions of southern Africa are determined by asymmetrical changes in the midlatitude westerlies between the Atlantic and Indian Oceans.

1. Introduction

Year-to-year variations in rainfall across southern Africa have major consequences for human livelihoods and ecosystems through their impacts on drought, temperature, water supply, vegetation, and agriculture. Southern African rainfall distribution is marked by a strong seasonality over most of the subcontinent. Austral summer (October through March) is the main rainy season over much of southern Africa. The importance of the summer season, however, is decreasing from the northeastern to southwestern regions (approximately 31–34°S, 17–21°E), where rainfall occurs mainly during the austral winter months (May to August). Southern African rainfall also experiences strong interannual fluctuations, with recurrent wet and dry periods, in response to the coupled ocean-atmosphere modes of variability over the Pacific, Indian, and Atlantic Oceans.

Interannual variability (2–8 years) of summer rainfall is known to be primarily influenced by El Niño–Southern Oscillation (ENSO) [e.g., *Ropelewski and Halpert*, 1987, 1989; *Lindesay*, 1988; *Mason and Jury*, 1997; *Rouault and Richard*, 2005; *Kane*, 2009; *Crétat et al.*, 2012; *Ratnam et al.*, 2014; *Dieppois et al.*, 2015], especially from the so-called 1976/1977 climate shift [*Richard et al.*, 2000, 2001]. However, ENSO effects on southern African rainfall are nonlinear with more (less) marked dry (wet) anomalies during El Niño (La Niña) years [*Fauchereau et al.*, 2009]. They also respond to interactions between the interannual time scales and synoptic-scale variability [*Pohl et al.*, 2009; *Fauchereau et al.*, 2009]. For instance, *Cook* [2001] and *Ratnam et al.* [2014] proposed that El Niño generates atmospheric Rossby waves in the Southern Hemisphere which could be responsible for an eastward shift of the South Indian Convergence Zone (SICZ), where synoptic-scale rain-bearing systems

that affect southern Africa, such as tropical-temperate troughs (TTT), preferentially develop [*Todd and Washington*, 1999; *Todd et al.*, 2004; *Hart et al.*, 2012a, 2012b; *Macron et al.*, 2014]. El Niño also leads to a northward shift of the subtropical highs [*Cook*, 2004; *Vigaud et al.*, 2009], which is associated with high-pressure anomalies over the continent, suppressing convection and restricting wind flows toward southern Africa [*Mulenga et al.*, 2003; *Dieppois et al.*, 2015]. In contrast, interannual variability of winter southern African rainfall is related to the Southern Annular Mode (SAM) [*Reason and Rouault*, 2005], which displays northward/southward shifts in the subtropical high-pressure belt similar to those produced in summer by El Niño events [*Pohl et al.*, 2009], and this impacts on South Atlantic sea surface temperature (SST) [*Reason et al.*, 2002; *Reason and Jagadheesha*, 2005]. *Phillipon et al.* [2012] also highlight a positive influence of ENSO on winter southern African rainfall (more frequent dry/wet spells during El Niño/La Niña) since the late 1970s, which is also associated with shifts in the subtropical highs and midlatitude westerlies.

Decadal fluctuations have also been found in summer southern African rainfall [*Dyer and Tyson*, 1977; *Tyson*, 1986; *Mason and Jury*, 1997; *Malherbe et al.*, 2012; *Jury*, 2014]. Of particular importance is the interdecadal Dyer-Tyson cycle (18–20 years [*Dyer and Tyson*, 1977]). Comparing synoptic maps during wet and dry years in the core areas of the interdecadal cycle, i.e., in the northeastern regions of southern Africa, *Tyson* [1981, 1986] noted associations with changes in the meridional circulation between the South Atlantic and Indian Oceans, which may relate to variations in the subtropical ridge of the first zonal standing wave over the Southern Hemisphere. According to *Malherbe et al.* [2014, 2016], this could be consistent with atmospheric anomalies related to the SAM during the late austral summer (January-February-March (JFM)). A quasi-decadal cycle in summer southern African rainfall, which is particularly pronounced along the south coast of South Africa [*Tyson*, 1981, 1986], has also been identified. Using the same approach for the southern cape (a region sensitive to summer and winter rainfall systems), *Tyson* [1981, 1986] associated these quasi-decadal fluctuations with longitudinal changes in the location of the first ridge of standing wave 3. However, later studies examining the summer rainfall regions have described these quasi-decadal fluctuations as chaotic resonances of interannual variability [*Mason*, 1990; *Kruger*, 1999; *Reason and Rouault*, 2002]: this implies that decadal forcing may appear similar to that driven by ENSO at the interannual scale.

Previous studies on the decadal variability of southern African rainfall have focused only on the summer months. Also, discussions about potential mechanisms and processes have been limited. Oceanic and atmospheric data sets have evolved considerably since the first hypotheses proposed by *Tyson* [1981, 1986]. The choice of observed or reanalyzed data sets, which have to cover an extended period (at least a century) as homogeneously as possible in order to detect robust signals associated with decadal time scale of variability, is, however, still not well considered (cf. section 2.1). Meanwhile, Coupled General Circulation Models (CGCMs), which meet these criteria, substantially underestimate the magnitude of decadal to multidecadal variability in precipitation at the global scale [*Ault et al.*, 2012], probably due to difficulties in simulating all the processes contributing to the development of such time scales of variability in the tropical Pacific [*Ault et al.*, 2013] and in the North Atlantic [*Ba et al.*, 2014; *Menary et al.*, 2015]. In addition, most of the studies cited above are based on comparisons between two periods of approximately 10 years, which are too short to capture the decadal variability signals (roughly two and a half cycles [*Maraun*, 2006; *Schaefli et al.*, 2007]). They are thus likely to describe changes in interannual variability between two decades that are not necessarily related to decadal signals. In this context, discussing the quasi-decadal variability as a chaotic resonance of interannual variability remains questionable. Other studies have used a ~10 year running mean [e.g., *Mason*, 1990; *Kruger*, 1999; *Jury*, 2014; *Malherbe et al.*, 2014], which acts as a primitive low-pass filter (which does not fully suppress interannual variability) and therefore prevents considering the existence of several independent decadal time scales in southern African rainfall variability.

This paper aims to address these gaps by defining the changing characteristics of both summer and winter southern African rainfall and their specific teleconnections for the main time scale of climate variability. Using a time-space approach based on spectral analysis, this study therefore aims to (1) provide a better understanding of decadal signals, which are likely to interfere with forced anthropogenic climate changes, and thus help improve seamless predictions at both seasonal [*Palmer et al.*, 2008; *Beraki et al.*, 2014] and decadal time scales [*Keenlyside et al.*, 2008; *Kirtman et al.*, 2013] and (2) provide new insights in understanding the nonlinear interactions between large-scale modes of climate variability and southern African rainfall. This paper is organized as follows. In section 2, the data set and analysis methods are described. In section 3, we analyze the dominant time scales of summer and winter southern African rainfall fluctuations. We examine in section 4
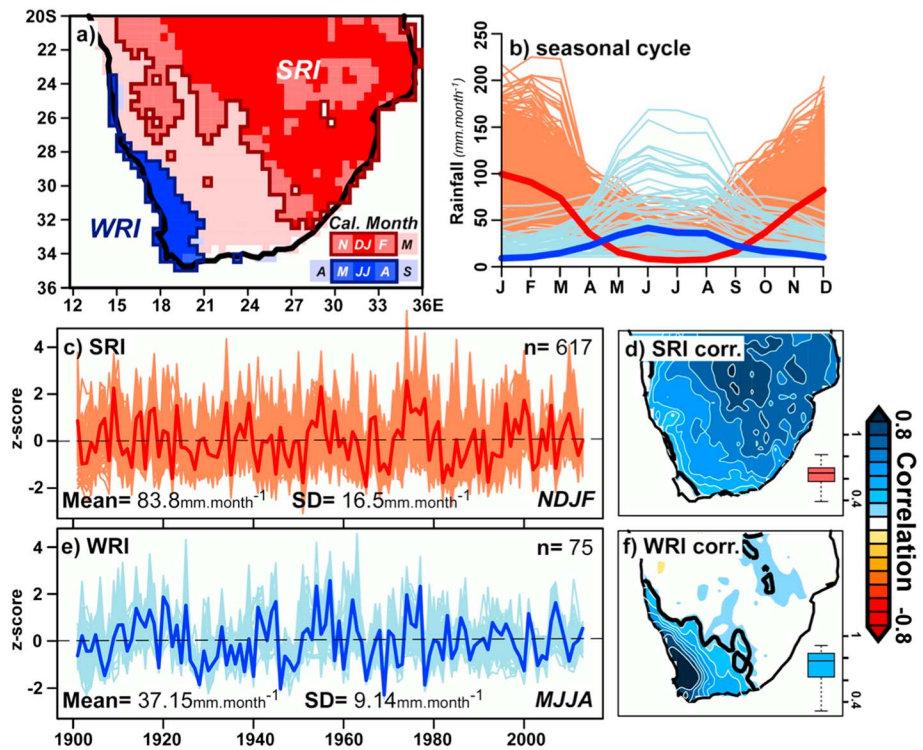
Figure 1. Seasonal patterns of southern African rainfall: time evolution and spatial coherence. (a) Spatial distribution of wettest month of the year over southern Africa (calendar month: red, November to March; blue, April to September). Bold lines delineate the area used for the calculation of summer and winter rainfall indices (SRI and WRI). (b) Annual cycles of summer (red: SRI) and winter (blue: WRI) southern African rainfall indices and of every grid points used for their calculations (light red and blue). (c) Interannual anomalies of SRI and all grid points used for its calculation ($n = 617$) over the 20th and early 21st centuries. (d) Pointwise correlation between interannual anomalies in the SRI and the CRU TS 3.23 rainfall field over southern Africa. Black contours indicate correlations significant at the 95% confidence level ($p = 0.05$). Box plot indicates the spatial spread in the correlation coefficients over the area used in computing the index. (e, f) as for Figures 1c and 1d but using WRI.

their teleconnections with global SSTs through each time scale of southern African rainfall variability before describing associated low-tropospheric to midtropospheric circulation anomalies in section 5 and upper tropospheric circulation anomalies in section 6. Our main results are interpreted and their wider implications are discussed in section 7.

2. Data and Methods

2.1. Data

The latest update of the Climatic Research Unit (CRU) data set is used to estimate southern African rainfall. The CRU TS 3.23 rainfall field is produced on a $0.5° \times 0.5°$ grid and is derived from monthly rainfall provided by about 4000 weather stations distributed around the world from 1901 to 2014 [*Harris et al.*, 2014]. As illustrated in Figures 1a and 1b, the wettest months occur between November and February (NDJF) in a major part of southern Africa (especially in the northeastern part), and between May and August (MJJA) in the southwestern and coastal regions (centered on the Western Cape region). While summer rainfall is primarily associated with synoptic-scale convective systems, such as tropical-temperate troughs (TTT) [*Hart et al.*, 2012a, 2012b; *Macron et al.*, 2014], winter rainfall is associated with the passage of westerly cold front systems [*Reason and Jagadheesha*, 2005]. The "all year" rainfall of the southern coastal regions has not been considered here due to its seasonal dependence on the climate processes driving summer and winter rainfall variability that affects substantially the interpretation of results. Therefore, two seasonal rainfall time series (winter and summer) have been constructed by averaging the values over two irregular regions. These describe the two main seasonal patterns, which are more clearly related to large-scale climate and circulation

modes of variability (Figure 1a): summer rainfall index (SRI in NDJF), and winter rainfall index (WRI in MJJA). Due to a substantial decline in the number of rain gauges used in CRU TS 3.23 data set from the mid-1990s, the quality of both seasonal indices is reduced over the last 20 years (Figure S1 in the supporting information). Over the first half of the twentieth century, however, the number of rain gauges over the summer and winter rainfall regions is considered to be good (Figure S1). Nevertheless, we estimated the dependency of the rainfall data sets using the centennial Global Precipitation Climatology Centre full data reanalysis version 7.0 (GPCC.v7) [*Schneider et al.*, 2014]. The correlations between rainfall indices from the CRU TS 3.23 and GPCC.v7 are, regardless of time scale, greater than 0.96 (significant at $p = 0.05$). This ensures similar patterns and timing of long-term rainfall variability and thus similar composite climate anomalies (Figures S2 and S3).

The spatial coherence of interannual rainfall anomalies of both indices has been assessed during their corresponding season (SRI in NDJF and WRI in MJJA; Figures 1b–1f). The annual peak of rainfall is distinctly well phased for both regions (Figure 1b). With respect to interannual rainfall anomalies, the median of the correlations between both regional indices and each grid point used for their calculation (within the dark red and blue boxes in Figure 1a; n[SRI/WRI] = 617/75) is approximately 0.65 and 0.78 (and significant at $p \leq 0.05$) for the SRI and the WRI, respectively (Figures 1d and 1f). The range of correlation coefficients is larger for the WRI, as displayed by the box plots (Figures 1d and 1f). Next, based on a pointwise correlation with the high-resolution rainfall grid over 34°–20°S and 10°–36°E, interannual SRI and WRI anomalies are both significantly correlated at $p = 0.05$ with a large patch over their calculation domains (Figures 1d and 1f). Maximum correlations occur within the calculation domains, i.e., northwest of Johannesburg for the SRI and north of Cape Town for the WRI (Figures 1d and 1f). Although lower for the WRI than for the SRI, a robust spatial coherence is suggested for both indices.

To examine the summer and winter teleconnections with global SSTs, we used the latest version of monthly SST data from the extended reconstructed SST (ERSST.v4) of the National Climatic Data Centre (NCDC). This ERSST.v4 gridded data set is generated using in situ data from the Comprehensive Ocean-Atmosphere Data Set (COADS) release 2.5, which employs new bias adjustments, quality control procedures, and analysis methods allowing for a reconstruction of sparse data over a 2° × 2° resolution grid [*Huang et al.*, 2015]. As for version 3b, version 4 does not use satellite data. It is thus coherent over the whole time period. In particular, it is not affected by a cold SST bias induced by the use of satellites at the end of the twentieth century [*Reynolds et al.*, 2002]. The use of satellite data leads to a modest decrease in the global warming trend, and thus probably of decadal signals, especially in the middle and high latitudes of the Southern Hemisphere [*Reynolds et al.*, 2002]. Uncertainty related to the SST data sets, which is largely associated with the difference of bias adjustments and interpolation techniques to handle sparse data in the Southern Ocean, is assessed in supporting information using the HadISST1 data from the Met Office Hadley Centre [*Rayner et al.*, 2003] and the COBE SST2 data from the Japan Meteorological Agency [*Hirahara et al.*, 2014].

The Twentieth Century Reanalysis version 2 (20CR.v2) is used to infer monthly atmospheric dynamics [*Compo et al.*, 2006; *Compo et al.*, 2011]. The 20CR.v2 is a 56-member ensemble global reanalysis, and available since 1871, over a 2° × 2° resolution grid that assimilates only surface pressure and uses monthly SST and sea ice distributions as boundary conditions. Such modeling and data assimilation strategy that remains constant over the entire time period allows spectral decompositions in analyzing atmospheric circulation across different time scales with a reduced sensitivity to artificial shifts induced by ingesting new data sets (as is the case for NCEP/NCAR-1 reanalysis [*Poccard et al.*, 2000]). The density of the observational network, i.e., amounts of assimilated data, as well as the quality of the SST field used as boundary conditions, remains nevertheless an intractable problem. This is likely to reduce the quality of the reanalyses, and the consistency between its different members, for the first decades of the period [*He et al.*, 2016]. This uncertainty is addressed in supporting information by quantifying the similarity between the ensemble mean and each individual ensemble member and between the members themselves (Figures S4–S7). The larger (lower) the agreement (spread) between the ensemble members, the lower (larger) the reliability of the reanalyses should be, since low intermember disagreements are indicative of a common response to a common forcing (namely, assimilated data of boundary conditions).

Six parameters are used here: latent heat flux (LHF), meridional wind (v) and zonal wind (u), specific humidity (q), geopotential height (z), and outgoing longwave radiation flux (OLR) at nominal top of atmosphere.
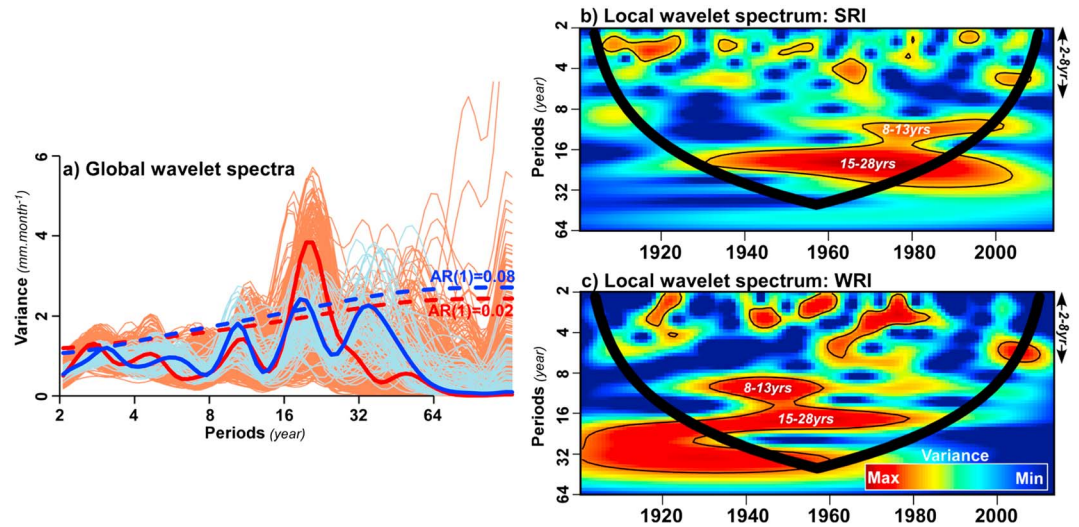
Figure 2. Time scale patterns of variability in summer and winter southern African rainfall. (a) Global wavelet spectra of the SRI (red) and the WRI (blue) and of every grid point used for their calculations (light red and light blue). The dashed blue and red lines indicate the red noise spectra with regard to the first-order autoregressive (SRI — AR[1] = 0.02; WRI — AR[1] = 0.08). (b, c) Continuous wavelet power spectrum of the SRI and the WRI. Bold lines (the so-called cone of influence) delineate the area under which power can be underestimated as a consequence of edge effects, wraparound effects, and zero padding; thin contour lines show the 95% confidence limits based on 1000 Monte Carlo simulations of the red noise background spectrum. SRI and WRI variability from the mid-1990s could be poorly represented due to a very low number of rain gauges available in the CRU TS 3.23 data set; this could substantially reduce interannual to interdecadal variability.

Low-tropospheric to midtropospheric circulation anomalies are described through geopotential height at 1000 hPa and mass-weighted vertically integrated moisture flux and convergence between the surface and 500 hPa $\left(\int_{ps}^{500 h Pa} \vec{V} q \text{ and } \int_{ps}^{500 h Pa} - \text{div.} \vec{V} q \right)$.

Upper tropospheric circulation anomalies are examined through OLR and wind circulation at 200 hPa.

2.2. Exploring Multiple Time Scales of Variability and Teleconnections

In section 3, time scale analysis is carried out using continuous wavelet transforms in order to visualize potential changes in the spectral content of each rainfall time series, i.e., the SRI and the WRI [e.g., *Torrence and Compo*, 1998; *Grinsted et al.*, 2004; *Maraun*, 2006; *Sang*, 2013]. By representing the time series into time scale domain, one can determine which scales of variability (or periods in a Fourier sense) are the dominant variability modes affecting SRI and WRI. Such decomposition of the monthly precipitation signals is conducted with a Morlet mother wavelet with angular frequency 6 to produce the local wavelet spectra (or global wavelet spectra in scale dimension only), which produces a good trade-off between time and frequency resolution [*Farge*, 1992; *Torrence and Compo*, 1998]. The significance test of the wavelet spectrum for geophysical signals assumes a red noise background spectrum for the null hypothesis, which is tested by Monte Carlo simulations of first-order autoregressive (AR[1]) processes. To minimize edge effects and to avoid wraparound issues, the time series are padded with zeroes. The cone of influence, which delineates the area under which power can be underestimated as a result of edge effects and zero padding, is therefore represented on all spectra here as a black bold line [*Torrence and Compo*, 1998] (Figure 2b).

The significant time scales of SRI and WRI variability are then reconstructed using fast Fourier transform (FFT) band-pass filtering, which can be considered as a digital filter in frequency domain. To reduce trend effects, both indices are first detrended using a locally weighted linear regression, with span equal to the length of the data. A nonzero mean and the trend term may otherwise affect the results [*Wu et al.*, 2007]. The power of the dominant modes of variability can then be compared over time on an orthogonal basis, and different metrics can be computed (cf. section 3).

In sections 4 and 5, we examine the teleconnections between rainfall indices and the worldwide SSTs on the one hand and atmospheric circulation on the other hand. In each grid point from 1901 to 2013, the time
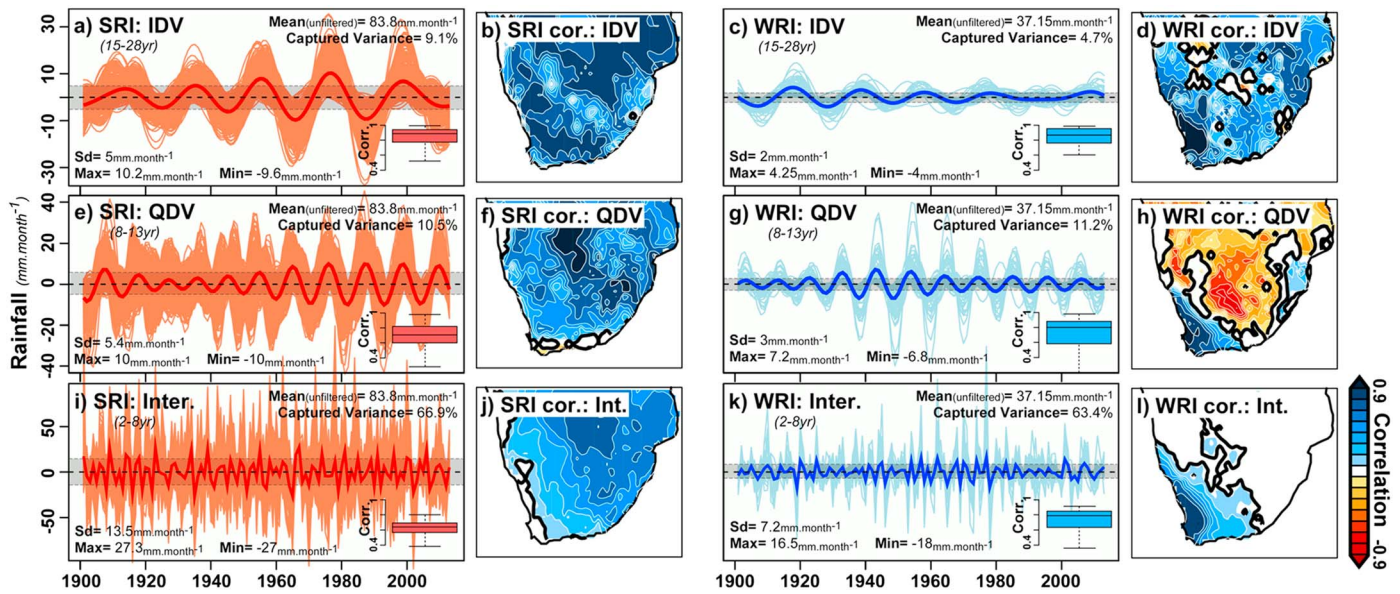
Figure 3. Reconstruction by FFT of dominant time scales modulating summer and winter southern African rainfall: contribution and spatial coherence. (a) Time evolution and statistics (captured variance in %, SD, Maximum, and Minimum) of interdecadal variability (IDV: 15–28 years) in the SRI (red) and all grid points used for its calculation (light red) over the twentieth century. The box plot indicates the range of correlation coefficients between the SRI and each grid point used for its calculation. (b) Pointwise correlation between the SRI and the CRU TS 3.23 at the interdecadal time scale. Black contours indicate correlations significant at $p = 0.05$. (c, d) As for Figures 3a and 3b but for the WRI (blue) and all grid points used for its calculation (light blue). (e–h) As for Figures 3a–3d but for the quasi-decadal time scale (QDV: 8–13 years). (i–l) as for Figures 3e–3eh but for the interannual time scale (2–8 years). The grey shaded bands delineate the area above which rainfall anomalies greater than ±1 SD have been selected to perform composite analysis.

series are detrended and next subjected to the FFT filter according to the significant time scales of southern African rainfall variability. Composite analysis is then performed to construct typical states of SSTs and atmospheric circulation. Two sets of SST and atmospheric anomalies are thus produced for each time scale, when rainfall variability is greater than ±1 standard deviation (cf. anomalies outside grey shaded band in Figure 3), after which the statistical significance is estimated by testing the difference in mean using a two-sided Student's t test at $p = 0.05$. When the time series were serially correlated, the degrees of freedom were adjusted by recalculating the "effective sample size" (N^{eff}). This is given by the following approximation [*Hamed and Rao*, 1998; *Yue and Wang*, 2004]:

$$\frac{N}{N^{eff}} = + \frac{2}{N(N-1)(N-2)} \sum_{i=1}^{t} (N-i-1)(N-i-2)\mathrm{ts}(i)$$

where N is the number of observations in the sample, $\mathrm{ts}(i)$ is the autocorrelation between ranks of the observations for lag i, and t is the maximum time lag under consideration. Dominant time scales of variability of key global climate indices have also been discussed using continuous wavelet analysis, while their statistical linear relationships with southern African rainfall have been assessed using wavelet squared coherence analysis [*Torrence and Webster*, 1999; *Maraun*, 2006].

Furthermore, ENSO variability is known to influence SST in the North Pacific [*Latif and Barnett*, 1994; *Pierce*, 2002; *Schneider and Cornuelle*, 2005], Atlantic [*Enfield and Mayer*, 1997; *Klein et al.*, 1999; *Czaja et al.*, 2002; *Toniazzo*, 2009], and Indian Oceans [*Tourre and White*, 1995; *Klein et al.*, 1999], as well as atmospheric circulation in the Southern Hemisphere [*Cook*, 2004; *Fogt and Bromwich*, 2006; *L'Heureux and Thompson*, 2006; *Vigaud et al.*, 2009; *Pohl et al.*, 2010]. We therefore performed a statistical sensitivity experiment, by removing ENSO influence from every climate anomaly, to disentangle the interactions involved properly. The first EOF (empirical orthogonal function) of tropical Pacific SST (35°S–35°N/120°E–60°W) has thus been generated, without applying band-pass filtering, for each season (NDJF and MJJA) and, then, statistically removed from the global SST and atmospheric data by subtracting linear regressions with the related principal component (PC). Induced modifications in SST and atmospheric anomalies would therefore be, at least partially, linearly associated with ENSO or decadal ENSO-like variability, and vice versa. Similarity between climate anomalies,

which are identified before and after linearly subtracting ENSO, has been quantified at the global scale by computing spatial correlations and evaluating the significance using *Dutilleul*'s [1993] modified *t* tests which account for spatial autocorrelation [*Clifford et al.*, 1989].

3. Dominant Time Scale of Southern African Rainfall Variability

Time scales of summer and winter southern African rainfall variability appear similar according to the global wavelet spectra (Figure 2a). According to the local wavelet spectra, interannual (2–8 year), quasi-decadal (8–13 year; QDV), and interdecadal (15–28 year; IDV) time scales are significantly above the red noise background spectra for both (Figures 2b and 2c). A distinct separation or spectral gap between the interdecadal and quasi-decadal signals is evident in Figures 2b and 2c; this is even more pronounced when enhancing the frequency resolution in the wavelet transform (Morlet wavelet order >6; not shown). Timing of periods of increasing variance at the interdecadal and quasi-decadal scales is different between summer and winter (SRI and WRI; Figures 2b and 2c). The SRI displays significant increasing variance since the 1930s at the interdecadal time scale and since the late 1960s at the quasi-decadal time scale (Figure 2b). Meanwhile, the WRI shows higher variance before the 1980s and the 1960s, and then decreases at interdecadal and quasi-decadal time scales, respectively (Figure 2c).

The SRI and WRI are then decomposed with FFT (cf. section 2.2), where each time scale of variability is displayed as rainfall anomalies, i.e., deviation from the mean of unfiltered data (SRI/WRI: 83.8/37.15 mm month^{-1}; Figure 3). Different metrics are calculated to evaluate their influence on seasonal rainfall amounts and fluctuations. Each rainfall index shows a robust spatial coherence over each time scale inside its calculation domain, with median correlation coefficients above 0.61 (and significant at $p \leq 0.05$; box plots in Figure 3). The range of correlation coefficients is higher at the quasi-decadal time scale in both indices. We then examined the contribution of each time scale, here expressed as a percentage of total variance captured by the FFT filter on the overall rainfall variability (var[filtered data]/var[unfiltered data]). Interestingly, the interannual scale emerges unambiguously as the dominant mode of variability over both summer and winter regions, with a contribution of about 63.4–66.9% (against less than ~11% for the quasi-decadal and interdecadal scales; Figure 3).

Interdecadal variability (15–28 years; IDV) displays fluctuations of about ± 5 and 2 mm month^{-1}, with maximum amplitude of fluctuations (maximum plus minimum) of about 19.8 and 8.25 mm month^{-1} in the SRI and the WRI, respectively (Figures 3a and 3c). Although the timing of enhanced interdecadal variability is different, interdecadal SRI and WRI anomalies are correlated with similar regions over southern Africa (Figures 3b and 3d). Quasi-decadal fluctuations (8–13 years; QDV) and interdecadal fluctuations are of the same order of magnitude (Figures 3e and 3g). At these time scales, the SRI is positively correlated over most of southern Africa, with the exception of the southern coastal regions (Figure 3f). Furthermore, the WRI is positively correlated with a large patch over their calculation domains but also negatively correlated with the rest of southern Africa (Figure 3h). Interannual variability (2–8 years) shows fluctuations of about ± 13.5 and 7.2 mm month^{-1}, with maximum amplitude of fluctuations of about 54.3 and 34.5 mm month^{-1} in the SRI and the WRI, respectively (Figures 3i and 3k). Correlation patterns of interannual variability are almost the same as those obtained with unfiltered indices (Figures 1d and 1f) and constitute a large patch over their calculation domains (Figures 3j and 3l). Such results were expected regarding the percentage of variance captured by inverse FFT filtering, but this also demonstrates that results of comparing two 10 year periods will essentially describe changes in interannual variability between the two periods.

4. Multiscale Relationship With Global SSTs

Figure 4 shows typical states of summer and winter global SSTs, constructed using composite analysis and based on fluctuations of summer and winter southern African rainfall from interannual to interdecadal time scales.

Composite anomalies associated with different SST and rainfall data sets are mostly consistent and significantly correlated (Figure S2). Discrepancies are stronger for winter rainfall (especially in the Southern, Pacific, and Indian Oceans) and at the interdecadal time scale (IDV: 15–28 years; Figures S2 and S3). We focus below only on SST anomalies showing an agreement greater than 90% between data sets (Figure S3). This ensures that similar SST anomalies would be identified using the ERSSTv.4, HadISST1, COBE SST2, CRU TS 3.23, and GPCC. v7 data sets.
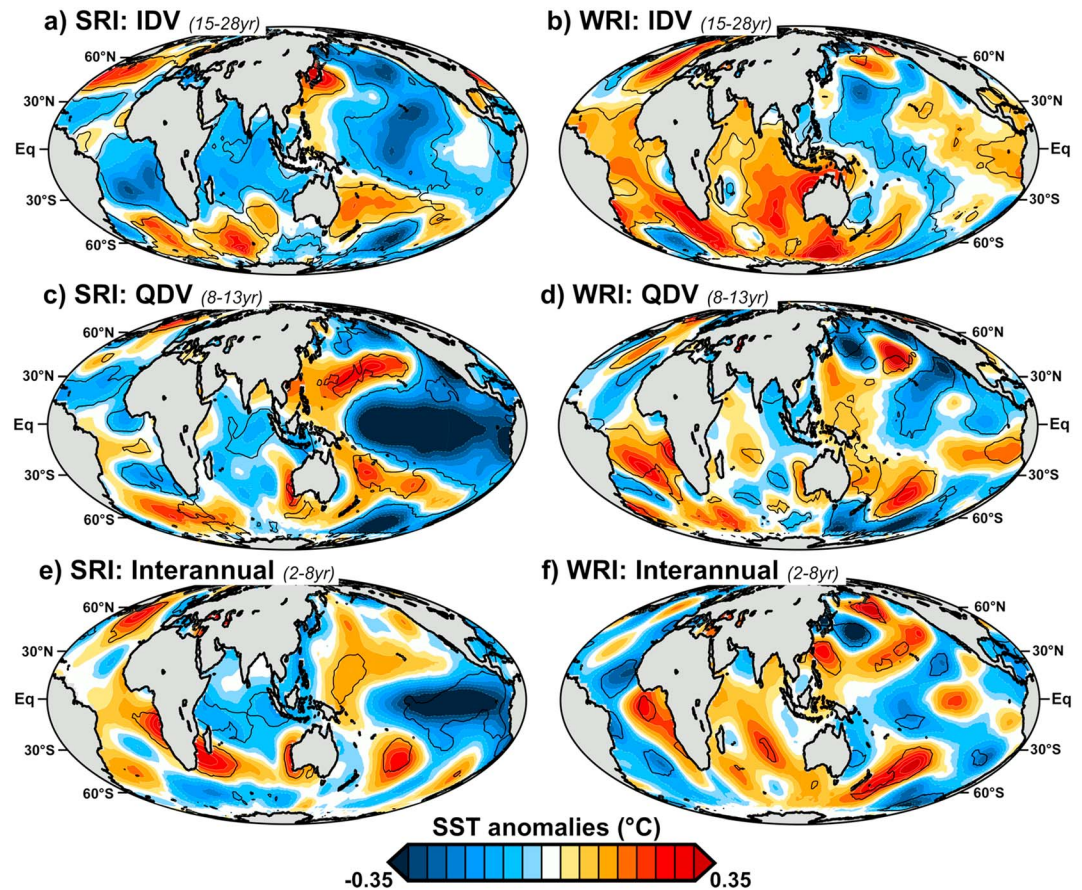
Figure 4. Summer and winter anomalies of SSTs associated with periods of high amplitude over the dominant time scales of summer and winter southern African rainfall variability, respectively. (a) Interdecadal composite anomalies of SSTs (in °C) during periods of enhancing interdecadal variability (IDV ≥ 1 SD) in the SRI. (b) As for Figure 4a but in the WRI. (c, d) As for Figures 4a and 4b but for the quasi-decadal time scale (QDV). (e, f) As for Figures 4c and 4d but for the interannual time scale. The statistical significance (black contours) has been estimated by testing the difference in mean between SST anomalies during periods of rainfall variability greater and lower than 1 SD (cf. anomalies outside grey shaded bands in Figure 3), through a modified t test accounting for pseudoreplication in the series at $p = 0.05$.

4.1. Summer Rainfall and Global SST Anomalies

At the interdecadal time scale (15–28 years; IDV), Pacific SST anomalies associated with positive SRI display a horseshoe pattern, with cold anomalies in the central North Pacific surrounded by anomalies of opposite sign east of Asia, off California, in the Alaska gyre, and in Southern Hemisphere extratropical regions (Figure 4a). This SST pattern is consistent with the interdecadal signals described by *Tourre et al.* [1999, 2001, 2005], and it is also reminiscent of the Pacific Decadal Oscillation (PDO) during its negative phase [*Mantua et al.*, 1997; *Minobe*, 2000; *Mantua and Hare*, 2002; *Mills and Walsh*, 2013]. Using the PDO index as defined by *Mantua et al.* [1997], significant interdecadal fluctuations are detected, and these are coherent with interdecadal SRI variability (Figure 5a). Such anomalies are still identified after linearly subtracting the influence of ENSO and decadal ENSO-like variability, hence the strong (significant at $p = 0.05$) spatial correlation coefficient between the two global SST patterns (Figure 6a). Some regional differences are identified, however. North Pacific anomalies are magnified in the extratropical and eastern equatorial regions, while they are weakened over western equatorial regions (Figure 6a). Two thirds of the PDO decadal variance is explained by zonal advection in the Kuroshio-Oyashio Extension and anomalies in the Aleutian low region [*Schneider and Cornuelle*, 2005]. Interactions between anomalies in the Kuroshio-Oyashio Extension, the Aleutian low region, and tropical convection are also proposed as a key driver of interdecadal climate variability in *Tourre et al.* [1999, 2001, 2005]. Positive interdecadal anomalies in the SRI are also related to cold anomalies in the tropical Indian Ocean and South Atlantic, while warm anomalies are detected in the extratropics
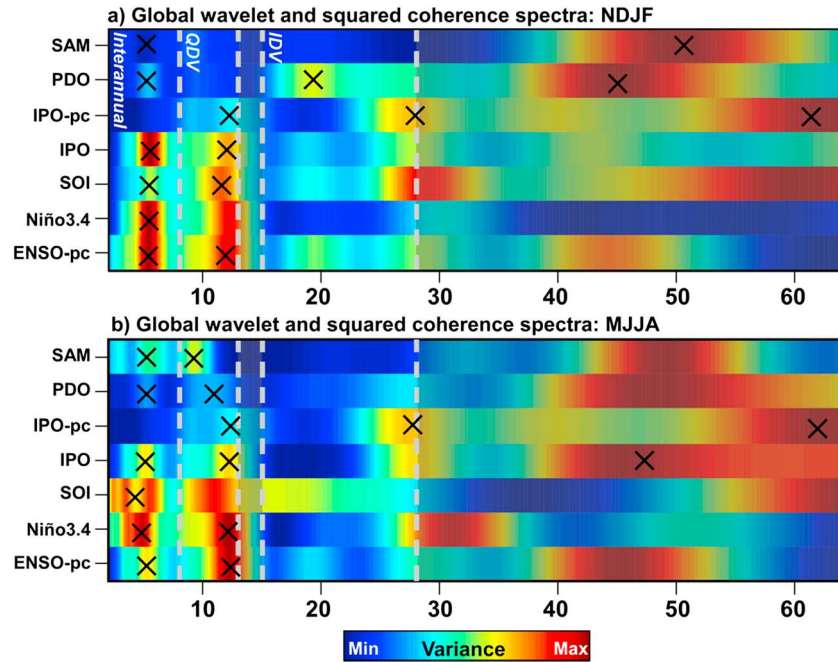
Figure 5. Time scale of variability in key global climate indices, and their statistical relationship with South African rainfall. (a) Comparison of global wavelet power spectrum in six global climate indices during summer, and their wavelet squared coherences with the SRI. (b) As in Figure 5a but in winter. The black crosses indicate the significant time scales and squared coherence at 95% confidence limits based on 1000 Monte Carlo simulations of the red noise background spectrum. Grey dashed lines delineate the three dominant time scales of South African rainfall variability. Seven global climate indices have been computed for each season using ERSST.v4 or 20CR.v2 data sets: (1) an ENSO-PC based as defined in section 2.2; (2) the Niño3.4 index; (3) the Southern Oscillation Index (SOI); (4 and 5) the tripole index for the Interdecadal Pacific Oscillation (IPO), which has been computed with or without 10 year low-pass filtering, as defined in *Henley et al.* [2015]; (6) the Pacific Decadal Oscillation (PDO) index as defined in *Mantua et al.* [1997]; and (7) the SAM index [*Thompson and Wallace*, 2000].

(Figure 4a). This defines the South Atlantic dipole, which is the dominant SST pattern in this region, in particular at interdecadal time scales [*Venegas et al.*, 1997], and the South Indian Ocean dipole [*Behera and Yamagata*, 2001]. This is consistent with CGCM experiments by *Morioka et al.* [2015], which show such influence of the South Indian Ocean dipole at decadal time scales. SST anomalies in the South Atlantic and South Indian Ocean are similar, after removing the influence of tropical Pacific SST variability (Figure 6a): this suggests, at least linearly, little impact of ENSO or decadal ENSO-like variability.

At the quasi-decadal time scales (8–13 years; QDV), Pacific SST anomalies associated with positive SRI fluctuations show cold anomalies in the tropical Pacific flanked by a horseshoe pattern of opposite sign, with marked anomalies in both North and South Pacific (Figure 4c). This SST pattern is consistent with the quasi-decadal signals described by *Tourre et al.* [1999, 2001, 2005] and is reminiscent of the Interdecadal Pacific Oscillation (IPO), which is a wide-basin pattern of ENSO, during its negative life cycles [*Zhang et al.*, 1997; *Power et al.*, 1999; *Folland et al.*, 1999]. This negative IPO occurs concomitantly with cold anomalies in the tropical Indian Ocean and SST dipole anomalies in the South Atlantic (Figure 4c). The physical and statistical independence between the IPO and ENSO is, however, debatable. This is evident when comparing the global wavelet spectra of different ENSO indices (ENSO-PC based, Niño3.4, and the Southern Oscillation Indices (SOI)) with the tripole index for the IPO defined by *Henley et al.* [2015], which display similar time scales of variability (Figure 5a). After linearly removing ENSO influence, tropical Indian and Pacific SST anomalies are strongly weakened, while extratropical SST anomalies do not change (except for the South Atlantic SST dipole, which is substantially weakened; Figure 6c). The spatial correlation coefficient between the two global SST patterns is 0.59 (Figure 6c). This supports earlier findings [*Tourre et al.*, 2005; *Power and Colman*, 2006], which showed that quasi-decadal fluctuations of equatorial Pacific SSTs, here related to the IPO, can be viewed as low-frequency ENSO phenomena. Only the tripole SST pattern in the North Pacific seems to be uncorrelated with the tropical Pacific SST variability (Figure 6c).
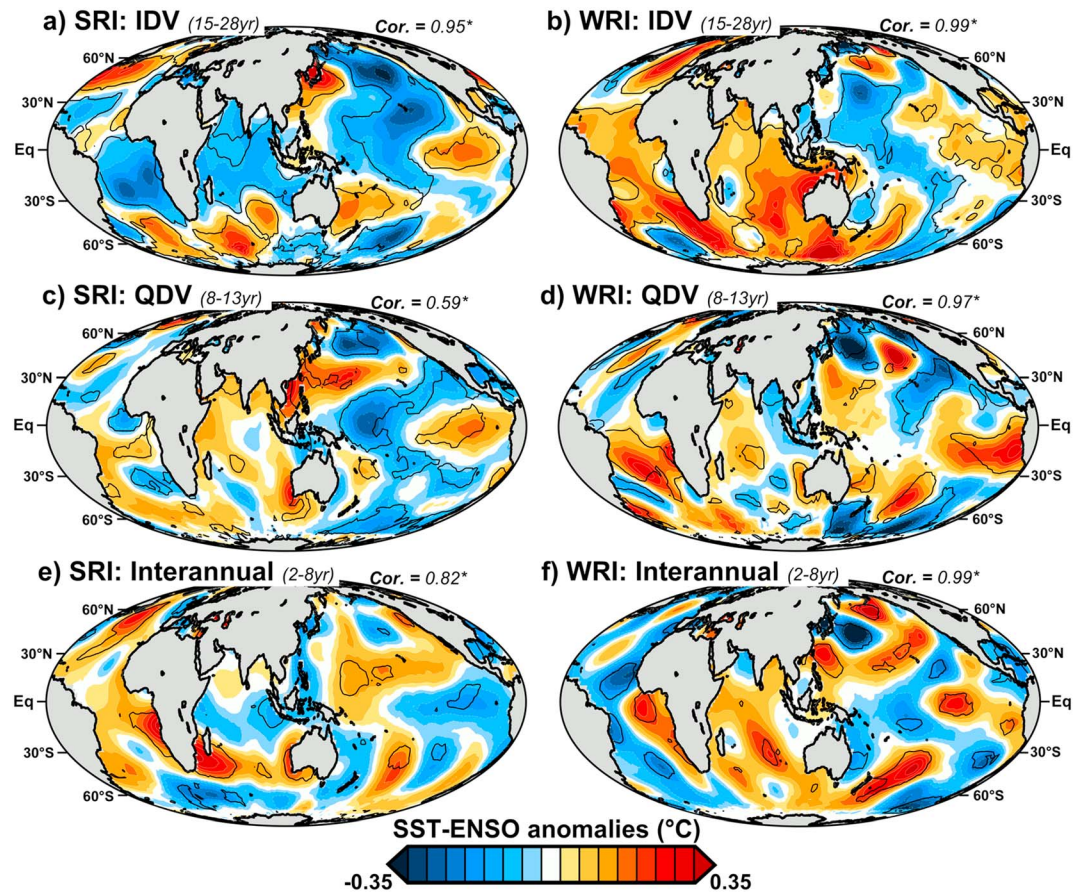
Figure 6. As for Figure 4 but after linear subtraction of ENSO influence. The spatial association between SST anomalies before and after removing the influence of ENSO has been quantified using a spatial correlation. Asterisks indicate significant spatial correlations at $p = 0.05$ with regard to Dutilleul's modified t tests accounting for spatial autocorrelation.

At the interannual scale (2–8 years), *Klein et al.* [1999] suggest that La Niña SST anomalies, which are associated with a cooler tropical Indian Ocean SST, are related to positive SRI anomalies. This suggestion is confirmed in Figure 4e and is consistent with the significant fluctuations and squared coherences identified in the ENSO indices at the interannual time scale (Figure 5a). Such anomalies are substantially weakened after linearly removing ENSO influence, indicating that they are strongly influenced by ENSO (Figure 6e). However, the ENSO footprint is not totally removed in the equatorial Pacific (Figure 6e), which highlights ENSO nonlinearity at the interannual time scale. The South Indian Ocean SST dipole is also identified in Figure 4e and appears to be magnified when ENSO influences are linearly removed (cf. Figures 4e and 6e). We also note a warmer tropical Atlantic in the northern Benguela upwelling region (Figures 4e and 6e), which is reminiscent of Atlantic Niños and Benguela Niños [*Lübbecke et al.*, 2010; *Rouault*, 2012].

4.2. Winter Rainfall and Global SST Anomalies

At the interdecadal time scale (15–28 years; IDV), Pacific SST anomalies associated with positive WRI anomalies are mostly centered on the North Pacific. Cold anomalies are detected over the southwestern and the central east North Pacific, contrasting with warm anomalies near the equator west of South America (Figure 4b). Although the equatorial warm anomalies do not seem to extend over the canonical ENSO footprint westward, this might indicate potential influences of decadal El Niño-like anomalies or of the Interdecadal Pacific Oscillation (IPO) during its positive phase [*Power et al.*, 1999; *Folland et al.*, 1999]. Significant interdecadal signals are indeed identified in the PC-based IPO index during winter (Figure 5b). However, all worldwide SST patterns are very similar with or without influences of tropical Pacific SST variability (spatial correlation = 0.99; Figure 6b), which suggests that ENSO or decadal ENSO-like patterns cannot be the main driver of interdecadal variability in the WRI. These SST anomalies are dominated by a

quasi-global SST warming in the Atlantic and in the Indian Ocean (Figures 6b and 5b). Meanwhile, dipole SST anomalies occur southwest of southern Africa (Figures 4b and 6b).

Pacific SST anomalies associated with positive quasi-decadal WRI fluctuations are centered on the northern regions and show warm anomalies being surrounded by cold anomalies in the southeastern and North Pacific (Figure 4d). Warm SST anomalies in the eastern equatorial Pacific, which can be influenced by decadal ENSO-like variability and/or the IPO, are also detected at the quasi-decadal time scale (Figures 4d, 5b, and 6d). However, after removing the influence of tropical Pacific SSTs, although the eastern Pacific SST anomalies are slightly enhanced, most global SST anomalies remain qualitatively unchanged (spatial correlation = 0.97; Figure 6d). Over the adjacent ocean, the South Atlantic SST dipole is identified (Figures 4d and 6d). Also, Indian Ocean SST anomalies display warm anomalies over the western tropical regions and cold anomalies over the eastern and extratropical regions (as far south as the latitude of Australia; Figures 4d and 6d).

At the interannual scale (2–8 years), positive WRI fluctuations are associated with sparse significant SST signals, which are unlikely to be distinguishable from a random noise. Significant SST anomalies are, however, identified in the North Pacific, i.e., cold anomalies east of Japan, which are surrounded by warm anomalies over the China Sea, off the Californian coast and south of the Bering Sea (Figures 4f and 6f). We also note warmer eastern tropical Atlantic and Indian Ocean SSTs, as well as cooler western Atlantic SSTs (Figures 4f and 6f). As for the longer time scales, global SST anomalies remain unchanged after removing ENSO influences (spatial correlation = 0.97; Figure 6f).

In summary, SST anomalies related to SRI and WRI are different for each time scale examined. SST anomalies associated with SRI fluctuations are substantially influenced by ENSO (especially at the quasi-decadal and interannual time scales). However, this is not the case for WRI. As suggested in *Wang et al.* [2014], the PDO might dampen or exacerbate ENSO-like anomalies, and, therefore, it could be an influential driver of summer rainfall in southern Africa. Interestingly, according to *Venegas et al.* [1997] and *Behera and Yamagata* [2001], both South Atlantic and South Indian Ocean SST dipoles can develop independently of ENSO (but remain nonlinearly influenced by the latter). They are also related to summer and winter South African rainfall.

4.3. Atmospheric Forcing on the SST?

This section discusses potential mechanisms resulting in the SST anomalies described in sections 4.1,4.2 through a literature review supported by composite anomalies of latent heat flux (LHF; Figure 7), as LHF is a key driver of many large-scale SST patterns [*Xie*, 2004]. Indeed, although the distribution of LHF anomalies is noisier than for SST, reduced LHF is related to warmer SST, while enhanced LHF is associated with cooler SST. This suggests that atmospheric variability is driving the SST. The opposite relation between latent heat flux and SST would suggest that the atmospheric variability damps the SST anomalies, although more complex relations could exist [*Xie*, 2004]. In addition, this relationship can even be more regionally complicated to understand where there is seasonal dependence of the role of ocean-atmosphere interaction dynamics, as it has been recently shown in the tropical Atlantic by *Nnamchi et al.* [2016].

For instance, on each time scale and using both summer and winter rainfall indices, South Atlantic and South Indian Ocean dipole SST anomalies are predominantly associated with LHF anomalies of opposite signs (Figures 4 and 7). This is not identified in summer at the interdecadal time scale (Figures 4a and 7a). Although 20CR reanalysis is forced by observed SSTs, such negative relationships between SST and LHF anomalies have been reported to result from one-way atmospheric forcing. As hypothesized in earlier studies [*Behera and Yamagata*, 2001; *Fauchereau et al.*, 2003; *Suzuki et al.*, 2004; *Hermes and Reason*, 2005; *Colberg and Reason*, 2007], such subtropical SST anomalies in the South Atlantic and South Indian ocean could be linked to changes in surface fluxes in response to changes in surface winds. According to *Vizy and Cook* [2016], this mechanism is also likely to explain the recent long-term decadal SST cooling anomalies over the subtropical South Atlantic, which could be linked to increased LHF from the ocean in response to a poleward shift of the westerlies and an intensification of surface wind speeds over this region. However, similar negative ocean-atmosphere Relationships have also been interpreted as feedback effects to the atmosphere. For instance, according to previous studies [*Reason*, 2002; *Washington and Preston*, 2006; *Morioka et al.*, 2015], the South Indian Ocean SST dipole could also induce, at the interannual and decadal time scales, an anomalous anticyclonic circulation driving an anomalous low-level easterly moisture flux toward southern Africa. *Morioka et al.* [2012, 2013] and *Vizy and Cook* [2016] also highlight the importance of year-to-year variations in the
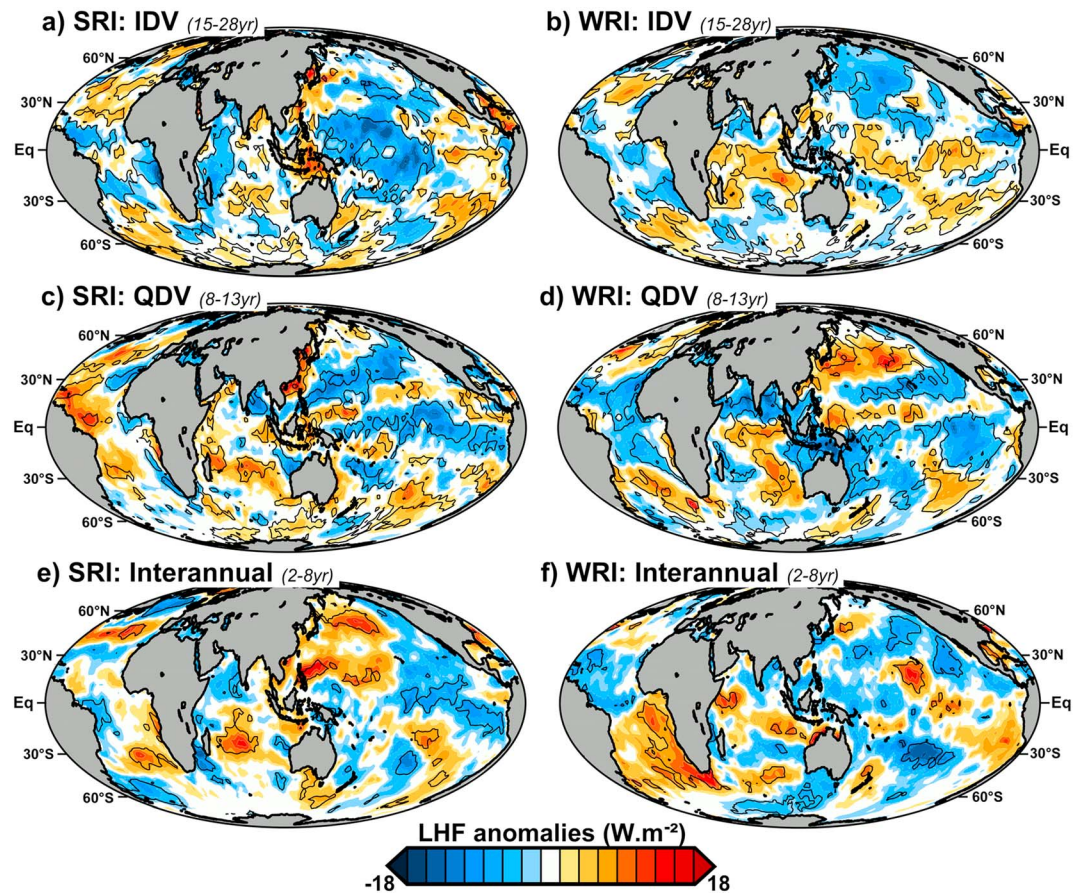
Figure 7. As for Figure 4 but for latent heat flux (LHF; in W m^{-2}).

mixed layer depth on the growth and maintenance of these SST anomalies. Such negative ocean-atmosphere interactions have also been identified in the North Pacific [*Nonaka and Xie*, 2003]. North Pacific tripole SST anomalies are thus associated with LHF of opposite signs at the quasi-decadal time scale in the SRI and interannual to quasi-decadal time scales in the WRI (Figures 4, 7c, 7d, and 7f).

Furthermore, positive relationships between SST and LHF anomalies can be identified in the eastern tropical Atlantic over the Benguela upwelling region, in the tropical western Indian Ocean, and in the eastern equatorial Pacific (Figures 4 and 7). The prevailing easterly trade winds have been reported to accelerate (decelerate) over warm (cold) SST by means of surface and latent and sensible heat fluxes [e.g., *Zhang and McPhaden*, 1995; *Hashizume et al.*, 2001; *Alexander et al.*, 2002; *Vecchi et al.*, 2004; *Xie*, 2004], which describes a clear SST influence on the atmosphere. *Vizy and Cook* [2016] thus noted that the poleward shift in the South Atlantic atmospheric circulation could also weaken coastal upwelling off the Angola Coast over the last three decades. Such positive ocean-atmosphere relationships have also been described in the North Pacific along the oceanic subarctic frontal zone [*Frankignoul and Kestenare*, 2002; *Tanimoto et al.*, 2003; *Taguchi et al.*, 2012]. As proposed by *Nonaka and Xie* [2003], this could also be identified in the Kuroshio and its extension, especially at the interdecadal time scale (Figures 4a, 4b, 7a, and 7b). Such positive ocean-atmosphere relationships are generally thought to be due to a vertical shear adjustment of the atmosphere near the sea surface [*Wallace et al.*, 1989; *Xie*, 2004].

5. Low-Tropospheric to Midtropospheric Circulation Anomalies

Figure 8 displays summer and winter means for geopotential height at 1000 hPa (z1000) and integrated moisture flux and convergence between the surface and 500 hPa $\left(\int_{ps}^{500 \ hPa} \vec{V} q \text{ and} \int_{ps}^{500 \ hPa} - \text{div.} \vec{V} q \right)$, which are compared to composite anomalies associated with each significant time scale of summer and winter rainfall variability. Figure 9 shows the same atmospheric composite anomalies after linear removal of ENSO influence.
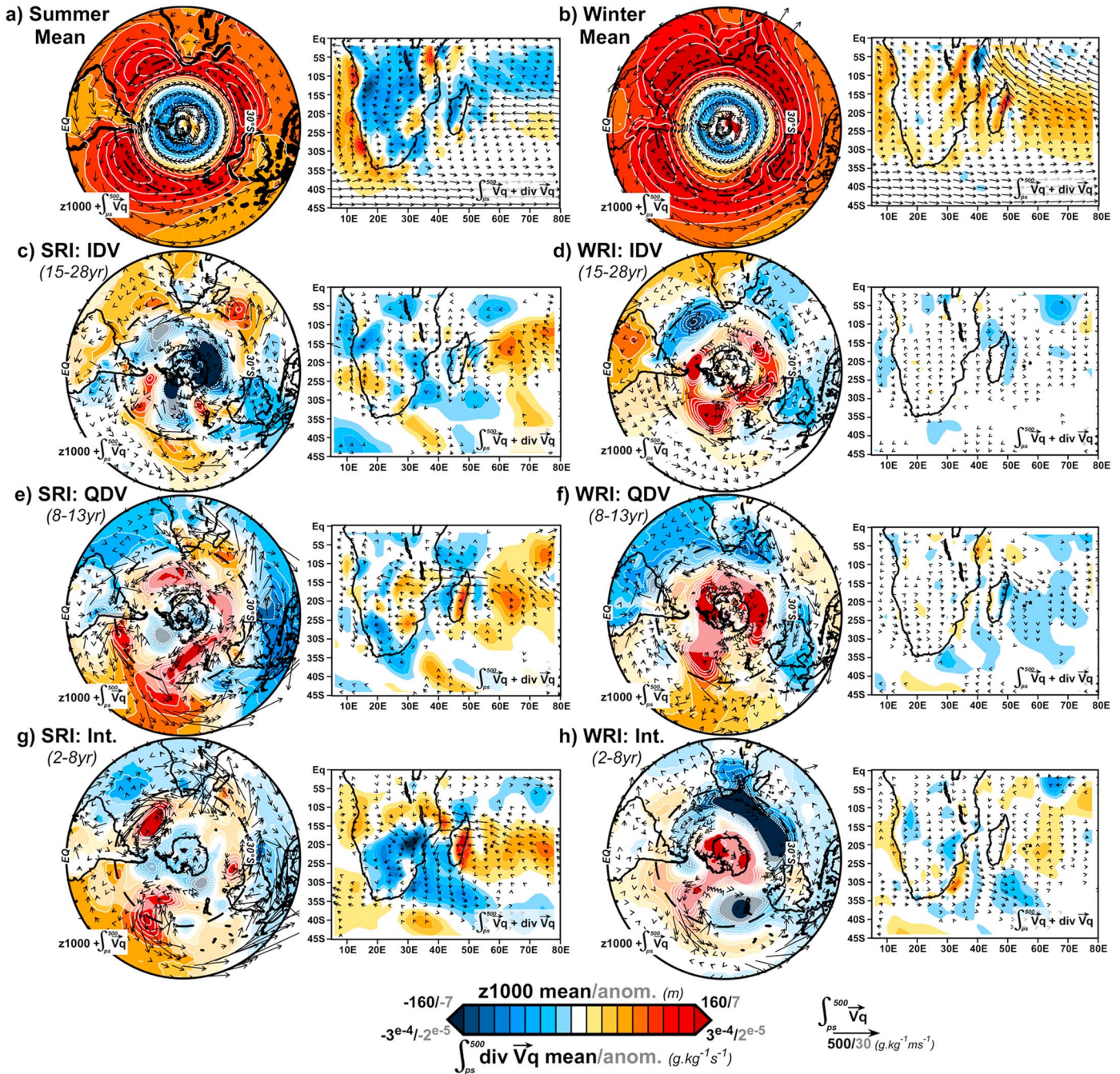
Figure 8. Anomalies of low-tropospheric to midtropospheric circulation during periods of high amplitude over the dominant time scales of summer and winter southern African rainfall variability. (a) Summer and (b) winter summer mean geopotential height at 1000 hPa (z1000 in m) and integrated moisture fluxes $\left(\text{arrows}, \int_{ps}^{500\ hPa} \vec{V} q \text{ in g kg}^{-1}\text{ms}^{-1}\right)$ and convergence $\left(\int_{ps}^{500h\ Pa} \vec{V} q \text{ in g kg}^{-1}\text{s}^{-1}\right)$ between the surface and 500 hPa. (c) Interdecadal composite anomalies of z1000, integrated moisture fluxes, and convergence during periods of enhancing interdecadal variability (IDV $\geq$ 1 SD) in the SRI. (d) As for Figure 8c but in the WRI. (e, f) As for Figures 8c and 8d but for the quasi-decadal time scale (QDV). (g, h) as for Figures 8e and 8f but for the interannual time scale. The statistical significance has been estimated by testing the difference in mean between atmospheric anomalies during periods of rainfall variability greater and lower than 1 SD (cf. anomalies outside grey shaded bands in Figure 3), through a modified t test accounting for pseudoreplication in the series at $p = 0.05$. Partial transparency has been used to mask nonsignificant z1000 anomalies, while only significant zonal or meridional integrated moisture flux anomalies are shown by arrows.
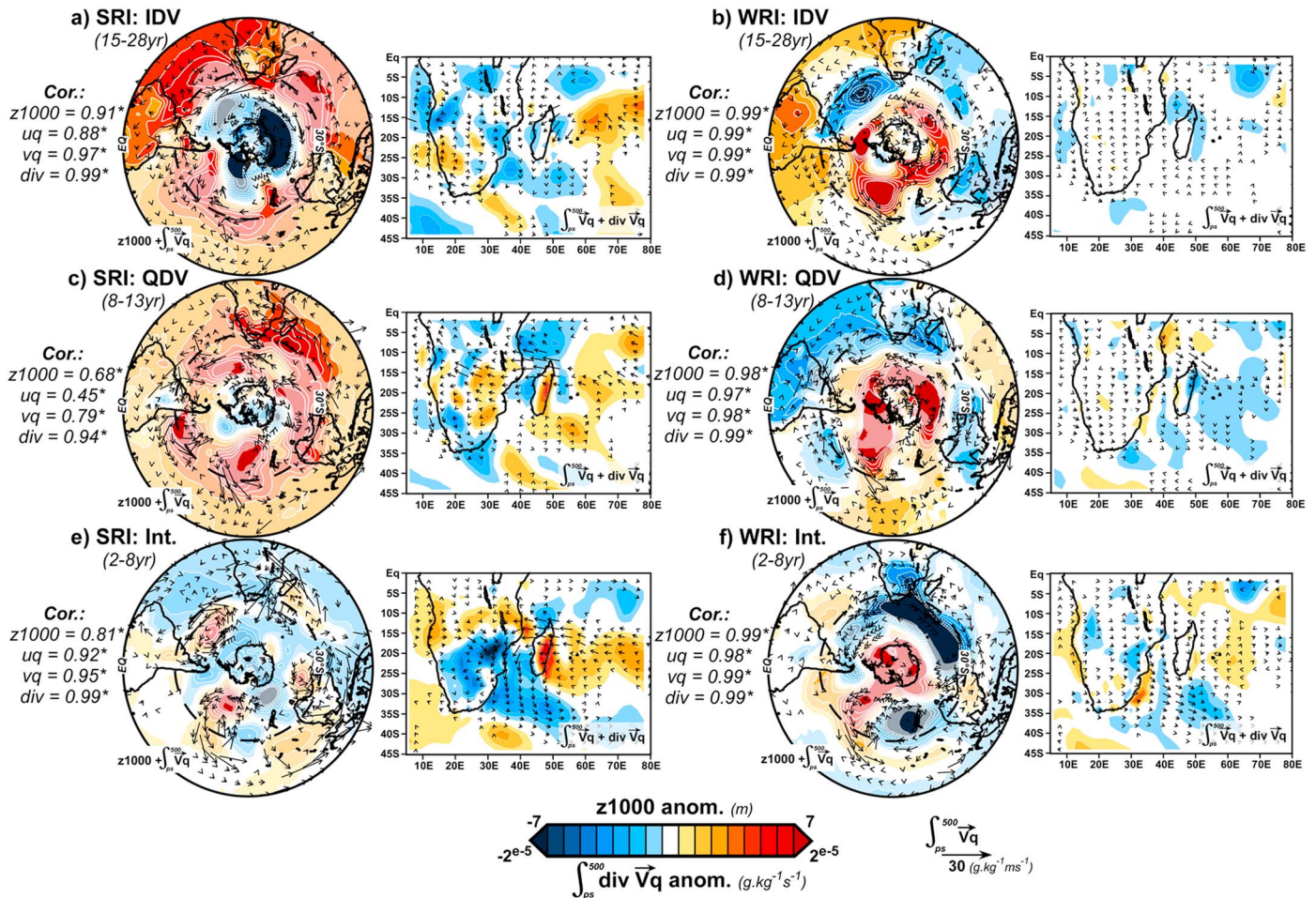
Figure 9. As for Figures 8b, 8d 8f, and 8h but after linearly subtracting ENSO influence. The spatial association between atmospheric anomalies before and after removing influences of ENSO has been quantified using a spatial correlation. Asterisks indicate significant spatial correlations at $p = 0.05$ with regard to Dutilleul's modified t tests accounting for spatial autocorrelation.

The z1000 composite anomalies were recalculated for all ensemble members to assess the consistency with those obtained using the ensemble mean and to test the robustness of the results with respect to the internal variability of the model. This provides a measure of the constraint of reanalyzed fields by assimilated data and thus a measure of the uncertainties in the atmospheric variables. Weak member dispersion denotes a strong reproducibility of a given climate signal, suggestive of a strong importance of input observations and, thus, possibly strong consistency between reanalysis and observed atmospheric patterns. At the global scale, geopotential height anomalies from all ensemble members are mostly consistent and significantly correlated to those from the ensemble mean (Figure S4a): this suggests that reanalyzed z1000 anomalies are strongly determined by the assimilation process and should result in generally consistent atmospheric fields against observations. Larger uncertainties are identified in summer at the interdecadal time scale and in winter at the interannual time scale (Figure S4a). Discrepancies between the members are stronger over Antarctica whatever the time scale and the season considered (Figure S5). Such internal variability, associated with a lower density of observational records available to constrain the model at the analysis time step, are nonetheless thought to have little effect on the patterns described in this section, since the member agreement is very strong for these patterns (Figure S5).

5.1. Summer Rainfall and Low-Tropospheric to Midtropospheric Circulation Anomalies

In Austral summer, the polar low extends up to 60°S, while high pressures occur in the tropics and subtropics (Figure 8a). Anticyclonic circulation associated with the South Atlantic and South Indian Highs is identified over the South Atlantic and South Indian Oceans, respectively (Figure 8a). The midlatitude westerly moisture

flux is thus evident between 37° and 60°S, but, on average, it is located too far to the south to directly influence southern African rainfall in Austral summer. According to *Crétat et al.* [2012] and *Pohl et al.* [2014], summer southern African rainfall over the northern regions (Mozambique, Malawi, Zambia, Angola, and northern South Africa) is primarily related to tropical convection within the Intertropical Convergence Zone (ITCZ). However, for the regions to the southeast, it relates more to the SICZ, which is formed from the convergence between the South Atlantic westerlies and the South Indian easterlies, farther southeast [*Cook*, 2000] (Figure 8a).

At the interdecadal time scale (15–28 years; IDV), low-tropospheric to midtropospheric circulation associated with positive SRI displays a quasi-annular mode, with low-pressure anomalies between the polar regions and 36°S and high-pressure anomalies in the subtropical and tropical regions (Figure 8c). A southward shift of subtropical westerly moisture fluxes, which is associated with a weakening of westerly moisture flows toward southern Africa, is identified for a large part of the Southern Hemisphere (Figure 8c). We also note an increase of anticyclonic circulation in the South Atlantic and South Indian high-pressure regions. This could be linked to a northward shift of the ITCZ, which is identified north of Madagascar from the Indian Ocean to the east of Lake Victoria (Figures 8c and 10b). These anomalies promote enhanced southerly moisture fluxes from the South Atlantic and, especially, easterly moisture fluxes from the southern Indian Ocean along 10–20°S toward southern Africa (Figure 8c). Low-pressure anomalies over the continent also favor moisture advections from the South Atlantic and Indian Oceans (Figure 8c). These converge over southern Africa and, thus, strengthen the SICZ (Figure 8c). Such anomalies are similar to those related to the SAM during its positive phase (spatial correlation = 0.51, significant at $p = 0.05$), but there is no significant interdecadal signal from November to February in the SAM index (Figure 5a). These quasi-annular anomalies were reported to show maximum spatial coherence and are more centered on Antarctica from January to March [*Malherbe et al.*, 2014, 2016], when the interdecadal variability in the SAM index is strongest and significant (not shown). In addition, although interdecadal anomalies are very similar before and after subtracting linearly ENSO and decadal ENSO-like effects (spatial correlation ≥ 0.88, significant at $p = 0.05$), subtropical/tropical high pressure is substantially enhanced (Figure 9a). This suggests a linear influence of ENSO on subtropical/tropical geopotential height anomalies, which reduces slightly easterly moisture fluxes and reduces rainfall due to increasing high pressure on the continent. Persistent easterly moisture fluxes related to anomalous anticyclonic circulation in the South Indian region are consistent with idealized model experiments of South Indian Ocean SST forcing, which is similar to that observed in Figure 4a, in HadAM3 [*Washington and Preston*, 2006]. As proposed by *Morioka et al.* [2015] through CGCM experiments, such decadal air-sea interactions could be interpreted as feedback effects to the atmosphere, which could help increase the persistence of regional shifts in the subtropical circulation.

At the quasi-decadal time scale (8–13 years; QDV), positive SRI anomalies are associated with an annular signal in the Southern Hemisphere, with weak low-pressure anomalies over Antarctica and in the tropics over the Atlantic and Indian basins, as well as high-pressure anomalies in the midlatitudes and tropical Pacific (Figure 8e). However, subtropical high-pressure anomalies are asymmetric between the Atlantic and the Indian Oceans, which suggest a southward shift of the South Atlantic High and an enhancement of the anticyclonic circulation in the South Indian High region (Figure 8e). High-pressure anomalies also occur over the southern parts of the continent (Figure 8e). An easterly moisture flux from the South Indian Ocean is thus identified over tropical southern Africa, which then moves toward the southwestern regions (Figure 8e). The moisture fluxes from the Indian Ocean converge with southeasterly moisture fluxes from the South Atlantic High, thereby strengthening the SICZ (Figure 8e). This relates to a northward shift of the ITCZ, north of Madagascar from the western Indian Ocean to central Africa (Figure 8e). These anomalies are suggestive of those driven by the SAM (spatial correlation = 0.48, significant at $p = 0.05$), but there is no significant quasi-decadal fluctuation in the summer SAM index (Figure 5a). After linearly removing the influence of ENSO and decadal ENSO-like variability, geopotential anomalies are substantially altered (spatial correlation = 0.68; Figure 9c). The quasi-annular pattern is weakened, while high-pressure anomalies are identified in the tropics and are enhanced in the subtropics (Figure 9c). High-pressure anomalies are thus detected over the continent, preventing rainfall and reducing easterly moisture fluxes (in particular between 50° and 80°E; Figure 9c). Summer rainfall variability at the quasi-decadal time scale is thus predominantly driven by the tropical dynamic linked to ENSO, decadal ENSO-like variability, or the IPO. In addition, the persisting easterly moisture fluxes could be related to the South Indian Ocean SST, as shown through atmospheric GCM and CGCM experiments, respectively, by *Washington and Preston* [2006] and *Morioka et al.* [2015].
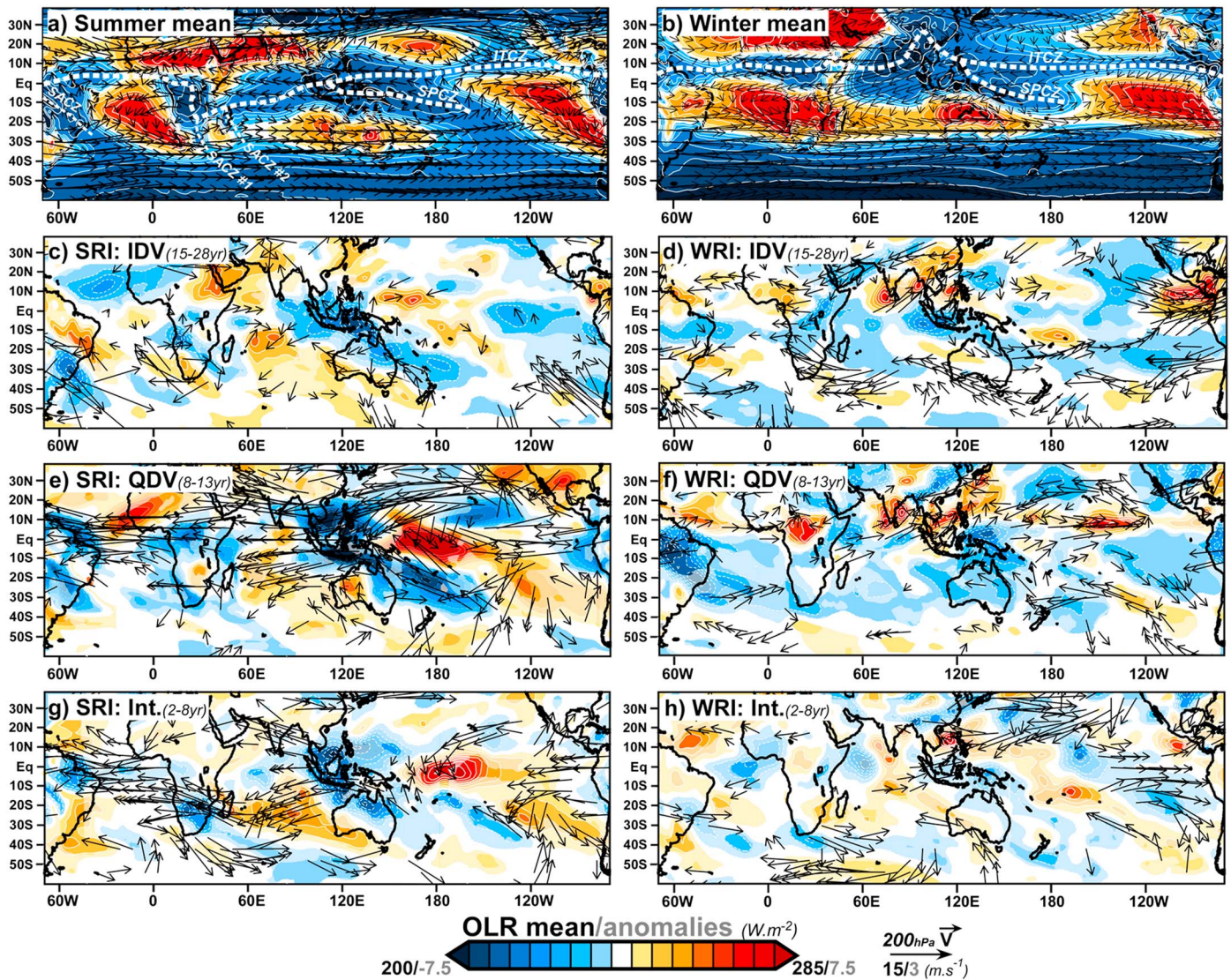
Figure 10. Anomalies of outgoing longwave radiation (OLR) and upper tropospheric circulation during periods of high amplitude over the dominant time scales of summer and winter southern African rainfall variability. (a) Summer and (b) winter summer mean OLR (in W m^{-2}) and wind circulation at 200 hPa (arrows, in m s^{-1}). (c) Interdecadal composite anomalies of OLR and wind circulation at 200 hPa during periods of enhanced interdecadal variability (IDV $\geq$ 1 SD) in the SRI. (d) As for Figure 10c but in the WRI. (e, f) As for Figures 10c and 10d but for the quasi-decadal time scale (QDV). (g, h) As for Figures 10e and 10f but for the interannual time scale. The statistical significance has been estimated by testing the difference in mean between anomalies during periods of rainfall variability greater and lower than 1 SD (cf. anomalies outside grey shaded bands in Figure 3), through a modified t test accounting for pseudoreplication in the series at $p = 0.05$. Partial transparency has been used to mask nonsignificant OLR anomalies, while only significant zonal or meridional integrated moisture flux anomalies are shown by arrows. Strong negative OLR anomalies (in blue) are associated with higher than normal clouds or more frequent cloud cover, while positive anomalies (in red) refer to suppressed convection.

At the interannual time scale (2–8 years), we note low-pressure anomalies in the tropical and polar regions, while asymmetric subtropical high-pressure anomalies occur between the Atlantic and Indian Oceans (Figure 8g). Such anomalies indicate a southward shift of the South Atlantic High and an enhancement of anticyclonic circulation in the South Indian High (Figure 8g). Southeasterly and easterly moisture fluxes reaching southern Africa are identified, in line with changes in the South Atlantic and South Indian atmospheric circulation, respectively (Figure 8g). They converge over southern Africa and thus reinforce the SICZ (Figure 8g). Concurrently, the ITCZ is shifted northward, as identified north of Madagascar over the Indian Ocean (Figure 8g). These anomalies, even though they are weak over Antarctica and reveal some zonal asymmetries in the midlatitudes, show some similarities with the summer SAM (spatial correlation = 0.58, significant at $p = 0.05$). Low-pressure anomalies in the tropical regions from the Atlantic to the western Pacific, which are associated high-pressure anomalies in the eastern tropical Pacific, also suggest an influence of

ENSO (Figure 8g). The spatial correlation between atmospheric circulation anomalies before and after subtracting ENSO influences is quite high at the hemispheric scale (spatial correlation ≥ 0.81; significant at $p = 0.05$; Figure 9e). This could be due to residual nonlinear ENSO impacts or to the combined impact of the SAM. However, after removing ENSO influence, there are no significant geopotential height anomalies at $p = 0.05$: this highlights the primary importance of ENSO at the interannual time scale. High-pressure anomalies over South Indian Ocean are weakened, which slightly reduces easterly moisture fluxes (Figure 9e). Feedback effects of SST anomalies to the atmosphere are also likely to contribute to maintaining shifted atmospheric circulation over the South Indian Ocean [*Reason*, 2002; *Washington and Preston*, 2006; *Morioka et al.*, 2015], even after subtracting ENSO effects. At the interannual time scale, however, the influence of ENSO on such anomalies is reversed compared to the interdecadal and quasi-decadal time scales.

5.2. Winter Rainfall and Low-Tropospheric to Midtropospheric Circulation Anomalies

In the Austral winter, the ITCZ is located farther north, which limits the influence of the tropics, and the SICZ is not discernible (Figure 8b). Subtropical high-pressure systems are strengthened, while the polar low is weakened (Figure 8b). This results in a strengthening of midlatitude westerly moisture fluxes, which also extend up to the southwestern and coastal regions (Western Cape region; Figure 8b). Winter rainfall is therefore primarily associated with the passage of westerly cold front systems [*Reason and Jagadheesha*, 2005].

Figure 8d shows that positive interdecadal WRI fluctuations are associated with a zonal geopotential pattern in the Southern Hemisphere, which is more pronounced in the South Atlantic. High-pressure anomalies are identified north of Antarctica, while low-pressure anomalies occur in the subtropics (Figure 8d). This indicates a weakening of the South Atlantic High, which is consistent with a northward shift of the subtropical westerlies in the South Atlantic (Figure 8d). An enhancement of westerly moisture fluxes toward the southwestern regions of southern Africa, which creates little convergence, is thus identified (Figure 8d). This is consistent with an increase in the midlatitude frontal activity. After linearly removing the influence of tropical Pacific SSTs, these geopotential anomalies are largely unchanged at the hemispheric scale (spatial correlation ≥ 0.99, significant at $p = 0.05$; Figure 9b). This suggests very little influence of ENSO on interdecadal winter rainfall variability, at least linearly.

At the quasi-decadal time scale (8–13 years; QDV), positive WRI anomalies are linked to an almost continuous and zonally symmetric annular pattern of positive geopotential height anomalies over the Southern Ocean. This is reminiscent of the SAM anomalies (spatial correlation $= 0.71$, significant at $p = 0.05$), which show a significant quasi-decadal variability during that season (Figure 5b). The South Indian High and the South Atlantic High are both weakened (Figure 8f). A northward shift in the midlatitude westerlies is identified over the South Atlantic and Indian Oceans and over the continent (Figure 8f). This is associated with enhanced midlatitude frontal activity and, thus, westerly moisture fluxes toward southern Africa and convergence over the southwestern and northeastern regions (Figure 8f). With this annular pattern are also associated contrasting geopotential height anomalies in the tropics, with high-pressure anomalies in the Pacific Ocean and low-pressure anomalies over the Atlantic Ocean and Australia (Figure 8f). While geopotential height anomalies are slightly modified after linearly subtracting the influence of ENSO, the global pattern does not change (spatial correlation ≥ 0.97, significant at $p = 0.05$). This suggests a specific influence of the SAM on the WRI at the quasi-decadal time scale. Quasi-decadal fluctuations, which are significantly coherent with those of the WRI, are indeed significant in the winter SAM index (Figure 5b). This lends useful support for the findings of *L'Heureux and Thompson* [2006] and *Pohl et al.* [2009], which show that the statistical relationship between the SAM and ENSO is strong only during austral summer and is not significant during the rest of the year.

At the interannual time scale (2–8 years), annular geopotential anomalies (composed of high-pressure anomalies over Antarctica and low-pressure anomalies in the subtropics) are linked to WRI fluctuations, suggesting influence of the SAM (spatial correlation $= 0.75$, significant at $p = 0.05$; Figure 8h), which shows a significant quasi-decadal variability during that season (Figure 5b). This geopotential signal is nevertheless stronger over the South Indian Ocean, which indicates a weakening of the South Indian High. A reinforcement of the midlatitude frontal activity is suggested by a northward shift in midlatitude westerlies, which is even more pronounced over the South Indian Ocean (Figure 8h). The resulting moisture flux primarily affects western to southwestern coastal regions of southern Africa, where it produces convergence (Figure 8h). At the hemispheric scale, low-tropospheric to midtropospheric circulation anomalies appear very
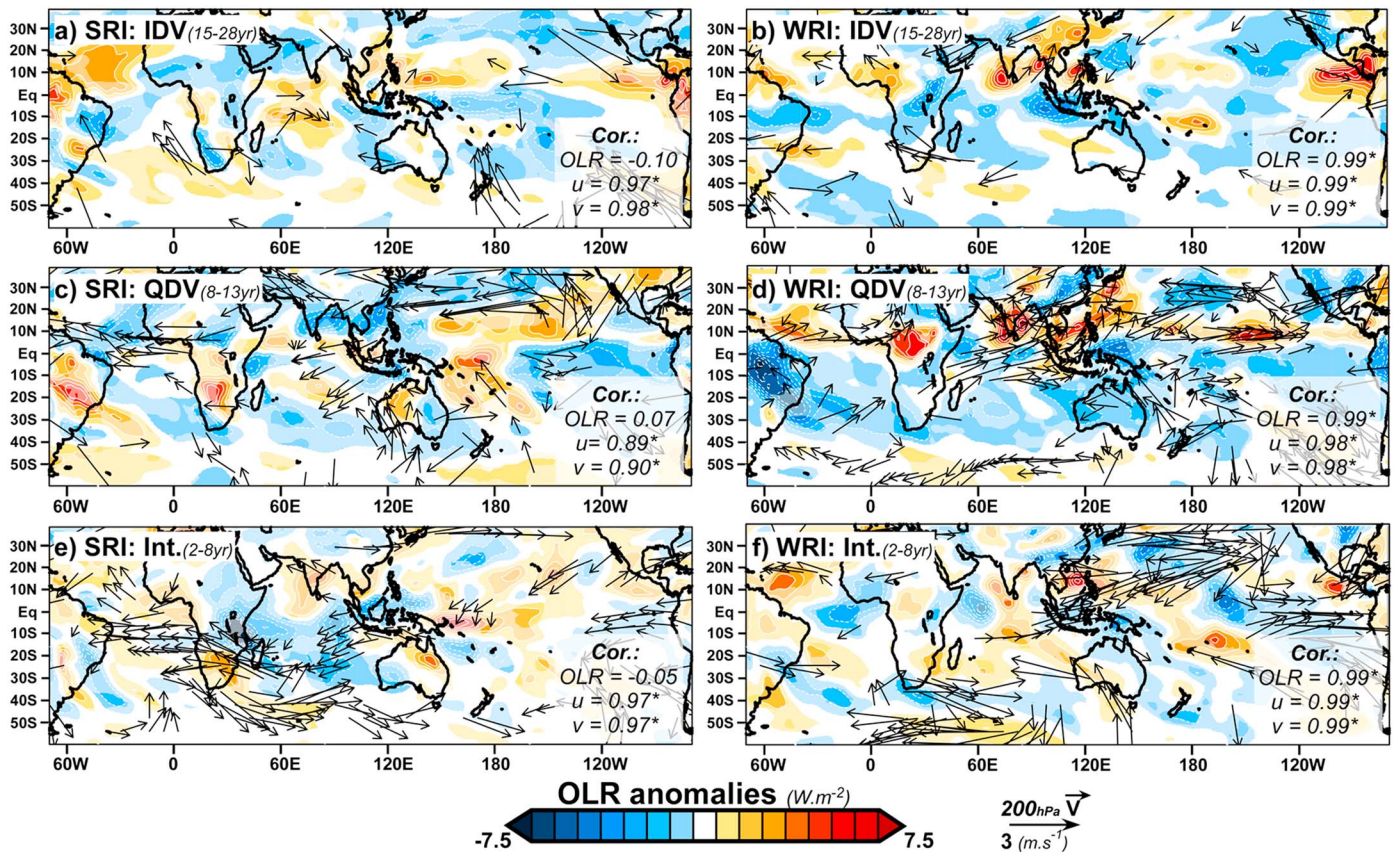
Figure 11. As for Figure 10 but after linearly subtracting ENSO influence. The spatial association between upper tropospheric anomalies before and after removing influences of ENSO has been quantified using a spatial correlation. Asterisks indicate significant spatial correlations at $p = 0.05$ with regard to Dutilleul's modified t tests accounting for spatial autocorrelation.

similar after linearly removing ENSO effects (spatial correlation ≥ 0.98, significant at $p = 0.05$; Figure 9f). This indicates a specific influence of the SAM on the WRI at the interannual time scale.

In summary, in summer, low-atmospheric to midatmospheric circulation anomalies are strongly influenced by ENSO, decadal ENSO-like variability, and their interactions with SST anomalies in the South Indian Ocean; in winter, however, they are mostly related to the SAM. As emphasized by earlier studies [*Seager et al.*, 2003; *Fogt and Bromwich*, 2006; *L'Heureux and Thompson*, 2006; *Pohl et al.*, 2010], the SAM itself is significantly correlated with ENSO in summer. The ENSO influence is stronger in the tropics and subtropics, and, according to *Fogt and Bromwich* [2006], this leads to asymmetrical geopotential anomalies between the South Atlantic and South Indian Oceans, which are likely to alter the canonical SAM pattern. This could be particularly true from January to February at the interdecadal time scale in accordance with *Malherbe et al.* [2014, 2016]. Interestingly, the influence of ENSO on the South Indian High is reversed between the interannual and the quasi-decadal to interdecadal time scales, which could highlight a time scale dependence of air-sea interactions. In winter, consistent with *Reason and Rouault* [2005], the influence of the SAM on southern African rainfall is strong and significant, particularly at the quasi-decadal and interannual time scales.

6. Upper Tropospheric Circulation Anomalies

Figure 10 displays summer and winter means for of 200 hPa wind circulation, as well as tropical/extratropical deep-convection anomalies (using OLR at the nominal top of atmosphere), which are compared to interdecadal to interannual composite anomalies. ENSO impact on such anomalies is then assessed by subtraction in Figure 11.

The OLR composite anomalies have been recalculated for every ensemble member to quantify the reproducibility of the results obtained with the ensemble mean. At the global scale, deep-convection anomalies from

all members are mostly consistent and significantly correlated to the ensemble mean (Figure S4b). This suggests that reanalyzed z1000 anomalies are rather strongly constrained by assimilated observations and result in rather low uncertainties according to the 20CR data set. Uncertainties are greater in winter (in particular at the interdecadal and interannual time scales; Figure S4b). The spread between the members is larger in the tropics in all seasons and time scales (Figure S6). The large-scale patterns interpreted in section 6.1, and based on the ensemble mean, are nonetheless strongly reproducible by all the members (Figure S7), implying uncertainties in the local and regional convective variability in the tropics rather than in large-scale patterns.

6.1. Summer Rainfall and Upper Tropospheric Circulation Anomalies

In Austral summer, the ITCZ is in its southernmost location at the global scale (Figure 10a). In particular, the ITCZ is parallel to the coast from central to southern Africa at approximately 30°E (Figure 10a). As mentioned in section 5.1, in summer, the ITCZ is the primary source of deep convection and rainfall over the northern regions of southern Africa. Farther south, summer rainfall is associated with tropical/extratropical deep convection in the SICZ [*Cook*, 2000] (Figure 10a), where synoptic-scale rain-bearing systems, such as tropical-temperate troughs (TTT), preferentially develop [*Todd and Washington*, 1999; *Todd et al.*, 2004; *Hart et al.*, 2012a, 2012b; *Macron et al.*, 2014]. However, unlike similar deep-convection features in the South Atlantic (South Atlantic Convergence Zone or SACZ [*Carvalho et al.*, 2004]) and in the South Pacific (South Pacific Convergence Zone or SPCZ [*Brown et al.*, 2013]), which occur throughout the year, the SICZ is only identified in Austral summer (Figures 10a and 10b). It is also characterized by a strong year-to-year spatial variability [*Cook*, 2000; *Fauchereau et al.*, 2009; *Pohl et al.*, 2009; *Crétat et al.*, 2012; *Macron et al.*, 2014; *Pohl et al.*, 2014]. Deep convection associated with the SICZ can thus be identified in a NW-SE direction over the continent (SICZ#1) or over the South Indian Ocean (SICZ#2; Figure 10a). Such interannual shifts in the mean location of the SICZ have been related to (1) phase changes in ENSO modes of variability (SICZ#1 in La Niña conditions and SICZ#2 in El Niño [*Cook*, 2001; *Fauchereau et al.*,2009]); and (2) Indian Ocean SST anomalies [*Nicholson*, 1997; *Nicholson and Kim*, 1997].

At the interdecadal time scale (15–28 years; IDV), positive SRI anomalies are associated with a west/east contrast of enhanced deep convection over the Maritime Continent and suppressed deep convection from the central to eastern Pacific (Figure 10c). These anomalies are much pronounced over the Southern Hemisphere than in the Northern Hemisphere (Figure 10c), but this could be consistent with a westward shift in the Walker circulation associated with a negative PDO. Suppressed deep convection is also seen over the SPCZ and the northward shifted ITCZ (Figure 10c). In the southern African domain, we identify in Figure 10c a large band of enhanced deep convection, being surrounded to the east and to the west by suppressed deep convection, with both extending in a NW-SE direction. This suggests a southwestward shift in the climatological location of the SICZ#2, which would be detected closer to the SICZ#1 location (Figure 10c). *Lyon and Mason* [2007] and *Hart et al.* [2012a, 2012b] argue that this shift of the SICZ#2 leads to enhanced development of synoptic-scale rain-bearing systems, such as the TTTs, over the northeastern regions of southern Africa at the synoptic scale. Interestingly, we find that after linearly removing the influence of decadal ENSO-like variability, such shifts in the longitudinal position of the SICZ#2 are reduced, while deep-convection anomalies occur in the region of the SICZ#1 (Figure 11a). This also highlights that although the PDO variability cannot result in a shift of the Walker circulation in the absence of tropical signals, this only partially influences the longitudinal changes in the location of the SICZ (Figure 11a). This tentatively suggests an additional forcing, such as interdecadal anomalies in the Indian Ocean SST, which are enhanced after subtracting the influence of decadal ENSO-like variability (Figures 4a and 6a). However, the intensity of deep-convection anomalies, which is substantially weakened, seems to be linearly related to decadal ENSO-like anomalies (spatial correlation $= -0.1$; Figure 11a). Also, a decrease of upper tropospheric westerlies due to a southward location of the midlatitude westerly jet is confirmed with or without the influence of tropical Pacific climate variability (Figure 10c). However, linear removal of the influence of ENSO does not modify the upper tropospheric wind circulation patterns at the global scale (spatial correlation ≥ 0.97, significant at $p = 0.05$; Figure 11a).

At the quasi-decadal time scale (8–13 years; QDV), positive SRI fluctuations are associated with similar upper tropospheric anomalies to those observed at the interdecadal time scale (Figures 10c and 10e). However, these anomalies are quite symmetric between the Northern and Southern Hemispheres (Figure 10e), which suggests an equatorial forcing such as decadal ENSO-like anomalies (here La Niña-like anomalies). A westward shift in the Walker circulation is identified and is associated, at the regional scale, with a southwestward

shift of the SICZ#2 toward the SICZ#1 location (Figure 10e). Interestingly, linearly subtracting the influence of decadal ENSO-like (such as the IPO) leads to a weakening of the shift in the Walker circulation and a reduction in the longitudinal shift of the SICZ (Figure 11c). Although deep-convection anomalies are substantially reduced over southern Africa after linearly removing the influence of decadal ENSO-like deep convection, anomalies persist in the region of the SICZ#1. At the quasi-decadal time scale, decadal ENSO-like variability contributes only partly to favor the development of synoptic-scale rain-bearing systems (e.g., TTTs), promoting wet conditions over the southern African landmass. The upper tropospheric wind circulation anomalies are weakened after removing the influence of tropical Pacific climate variability, but the pattern is largely unaffected (spatial correlations ≥ 0.87, significant at $p = 0.05$; Figure 11c).

Positive interannual SRI anomalies (2–8 years) are similar to those noted at the quasi-decadal time scale, but they are significantly less pronounced over the equatorial Pacific (Figures 10e and 10g). We thus identify a westward shift in the Walker circulation, which is associated with a southwestward shift from the SICZ#2 toward the SICZ#1 location (Figure 10g). This shift of the SICZ#2 is much less pronounced at the interannual scale than at the quasi-decadal scale (Figures 10e and 10g). At the quasi-decadal time scale, the shift in the Walker circulation is strongly weakened after linearly subtracting ENSO effects: this reduces the westward shift of the SICZ (Figure 11e). This is consistent with a weakening of the South Indian High after subtracting the influence of ENSO (Figure 9e). Although SST dipole anomalies in the Indian Ocean should partly contribute to shift the SICZ at the interannual time scale, this highlights the primary importance of ENSO in favoring the development of synoptic-scale rain-bearing systems (e.g., TTTs), which promote wet conditions over southern Africa. Furthermore, this also confirms a decrease in the intensity of the midlatitude westerly jet in response to the southward shift during wet conditions at the interannual scale (Figures 10g and 11e).

6.2. Winter Rainfall and Upper Tropospheric Circulation Anomalies

In Austral winter, as mentioned in section 5.2, the ITCZ is located farther north compared to summer, which limits the influence of the tropics (Figure 10b). Meanwhile, the midlatitude westerly jet is seasonally strengthened and slightly shifted northward (Figure 10b). Note that the Walker circulation is not evident in the summer and winter mean condition (Figures 10a and 10b).

At the interdecadal time scale (15–28 years; IDV), positive WRI fluctuations are associated with suppressed/enhanced deep convection, which is regionally identified north/south of the equator (~20°N–20°S) and of the subtropics (~20°–40°S; Figure 10d). This suggests regional changes in the tropical and subtropical meridional circulation, which are consistent with interdecadal zonal geopotential anomalies (Figure 8d). The subtropical westerly jet is shifted farther north in the South Atlantic and farther south over the Indian Ocean (Figure 10d). This pattern does change after linearly subtracting ENSO and decadal ENSO-like effects (spatial correlations ≥ 0.99, significant at $p = 0.05$; Figure 11b). This confirms a negligible influence of the tropical Pacific SST anomalies at the interdecadal time scale.

At the quasi-decadal time scale (8–13 years; QDV), upper tropospheric circulation anomalies are similar to those identified at the interdecadal time scale. OLR anomalies, which seem linearly independent of tropical Pacific climate variability, display suppressed convection in the ITCZ (and the midlatitudes too) and enhanced convection in the tropics (Figures 10f and 11d), indicating regional weakening in the meridional circulation. A northward shift and an increase of upper tropospheric westerlies is detected around 20–30°S in the South Atlantic (Figure 10f).

Positive interannual WRI anomalies are also associated with regional modifications in the meridional circulation. Suppressed/enhanced deep convection is regionally distributed north/south of the equator (~30°N–10°S) and of the subtropics (~10°–40°S; Figure 10h). A northward shift of the midlatitude westerly jet is detected around 20–40°S, which, with a large band of more frequent cloud cover, suggests increase in the westerlies between southern Africa and Australia (Figure 10h). As at the interdecadal and quasi-decadal time scale, these interannual anomalies are not modified after linearly removing ENSO effects (spatial correlation ≥ 0.99, significant at $p = 0.05$; Figure 11f), which confirms a negligible influence of the tropical Pacific SST anomalies.

In summary, at each time scale considered, tropical/subtropical teleconnections are the main drivers of SRI variability. Whatever the time scales specifically considered, these teleconnections are associated with scale interactions. In summer, the tropical Pacific climate variability which is linked to ENSO or decadal ENSO-like variability is associated with shifts in the Walker circulation: these serve (with non-ENSO-like ocean-atmosphere

anomalies in the South Indian Ocean) to modulate the intensity and longitudinal displacements of the SICZ and, thus, to influence precipitation over southern Africa. The mechanisms are more complex in winter, when the influence of the SAM, here expressed as shifts and intensifications of the midlatitude jet stream, becomes more important and ENSO becomes negligible. These new analyses here, therefore, show that winter teleconnections are associated with midlatitude and high-latitude dynamics, which can respond to, or be coupled with, regional changes in the meridional circulation. Similarities are, however, identified across time scales, which suggest interlocking mechanisms between them.

7. Discussion and Conclusion

This study analyzes the changing characteristics of summer and winter southern African rainfall and their teleconnections with large-scale climate through the dominant time scales of variability. Austral summer is the main rainy season over much of southern Africa, which occurs over the tropical and subtropical regions. However, in the southwestern tip of Africa, the annual rainfall peak occurs in austral winter. Two spatially coherent rainfall indices referred to as SRI and WRI have been calculated with respect to the two main seasonal patterns. As determined by wavelet analysis, both indices exhibit three significant time scales of variability: interdecadal (15–28 years), quasi-decadal (8–13 years), and interannual (2–8 years). Timing of periods of strong variance at the interdecadal and quasi-decadal time scales is nevertheless different for both rainfall indices. For instance, at the interdecadal and quasi-decadal time scales, the SRI displays significantly increasing variance since the 1930s and the late 1960s, while WRI shows decreasing variance.

Teleconnections with worldwide SST and atmospheric circulation anomalies impacting SRI and WRI fluctuations are different on all three time scales considered here. Importantly, the tropical/subtropical teleconnections emerge here as the main driver of summer rainfall variability at every time scale. Different timings between interdecadal, quasi-decadal, and interannual anomalies could thus provide some insights in understanding the nonlinear relationship between ENSO and southern African rainfall [*Fauchereau et al.*, 2009]. This might also help to understand the development of ENSO flavors [*Johnson*, 2013], as well as their contrasted impacts on southern Africa [*Ratnam et al.*, 2014; *Hoell et al.*, 2015]. Indeed, the development of ENSO flavors might, at least partly, result from interactions between Pacific SST anomalies occurring at different time scales (e.g., PDO SST anomalies influencing ENSO anomalies), although this has never been studied before. At the interdecadal time scale, ENSO or decadal ENSO-like forcing of the PDO decadal variance leads to shifts in the Walker circulation, which, at the regional scale, contribute with ocean-atmosphere anomalies in the South Indian Ocean to shift the SICZ#2 toward its continental position (SICZ#1). Combinations of ENSO forcing and ocean-atmosphere anomalies in the South Indian Ocean are thus needed in the relationship between PDO and southern African rainfall, as introduced by *Wang et al.* [2014], and this is supported by the new analyses presented here. The IPO and ENSO, whose physical independence remains controversial [*Power et al.*, 1999; *Folland et al.*, 1999; *Tourre et al.*, 2005; *Power and Colman*, 2006], also drive such anomalies at the quasi-decadal and interannual time scales. At each time scale, colder or warmer Pacific SSTs result in changes in the Walker circulation: these interact with ocean-atmospheric changes in the South Indian Ocean, which act together with varying degrees of importance to alter the intensity and longitudinal location of the SICZ and, thus, to modulate the TTT developments and deep convection over southern Africa.

At each time scale, these atmospheric changes in the South Indian Ocean are embedded in quasi-annular geopotential anomalies describing a southward shift in the midlatitude westerlies. These could be related to the canonical SAM pattern or ENSO-like anomalies in the Southern Hemisphere [*Seager et al.*, 2003; *Fogt and Bromwich*, 2006; *L'Heureux and Thompson*, 2006; *Pohl et al.*, 2010]. The relationship with the SAM is likely to be stronger from February to March at the interdecadal time scale in accordance with *Malherbe et al.* [2014, 2016]. Interdecadal to interannual variability in summer rainfall is thus closely related to an increase of easterly moisture fluxes from the South Indian High, which converges over the continent with southerly moisture fluxes from the South Atlantic High. In particular, the South Indian moisture fluxes are more pronounced than those from the South Atlantic at the interdecadal time scale, while, at the quasi-decadal and interannual time scales, the South Atlantic moisture fluxes are shifted southward compared to those from the South Indian Ocean. This asymmetry could contribute to explain why the SICZ is shifted longitudinally and enhanced. Such regional changes in the atmospheric circulation could be associated with dipolar SST anomalies in the adjacent oceans via changes in latent heat fluxes [*Behera and Yamagata*, 2001; *Reason*, 2002;

Fauchereau et al., 2003; *Suzuki et al.*, 2004; *Hermes and Reason*, 2005; *Washington and Preston*, 2006; *Colberg and Reason*, 2007; *Morioka et al.*, 2015; *Vizy and Cook*, 2016].

Our results show that the influence of tropical Pacific climate variability on southern African rainfall variability is almost negligible in winter over the twentieth century. However, according to *Phillipon et al.* [2012], the influence of tropical Pacific climate variability may have become more important since the 1970s. Although sparse significant signals have been detected at the interannual time scale, the interdecadal and quasi-decadal variability of winter southern African rainfall can be associated with SST anomalies in the North Pacific and more particularly with contrasted SST anomalies between the Atlantic and Indian Oceans, the sign of which depends on the time scale considered. These asymmetric dipole SST anomalies in the oceans adjacent to southern Africa are likely to be associated with changes in surface winds which would alter the turbulent latent heat and sensible heat fluxes. Winter rainfall variability is strongly related to regional changes in the subtropical highs and, thus, to midlatitude westerly frontal activity. *Reason and Rouault* [2005] argue that the influence of the SAM is strong in austral winter. We show that it influences quasi-decadal and interannual time scales of variability. According to OLR anomalies, this could be in response or coupled to regional modulations in the meridional circulation, although the main forcing of this modulation in the meridional circulation is not identified here.

This study provides new insights on climate interactions across different time scales and at global and regional scales and clarifies our understanding of decadal scale climate variability and predictability. By virtue of the methodology, which disentangles the processes of multiple time scales, this study provides a clearer synthesis of atmospheric dynamics associated with global ocean-atmosphere modes of variability which influence, seasonally and regionally, vital southern African rainfall receipts. Such analyses will help to understand recurrent rainfall and drought patterns across this dry region. Our results could thus be used to test the ability of Earth system models (e.g., Coupled Model Intercomparison Project-Phase 5 [*Taylor et al.*, 2012] as well as their future releases) to reproduce such teleconnections across distinct time scales. This issue is of particular importance in developing new seamless prediction approaches at the seasonal [*Palmer et al.*, 2008; *Beraki et al.*, 2014] to decadal time scales [*Keenlyside et al.*, 2008; *Kirtman et al.*, 2013].

References

Alexander, M. A., I. Blade, M. Newman, J. R. Lanzante, N.-C. Lau, and J. D. Scott (2002), The atmospheric bridge: The influence of ENSO teleconnections on air-sea interaction over the global oceans, *J. Clim.*, 15, 2205–2231.

Ault, T. R., J. E. Cole, and S. S. George (2012), The amplitude of decadal to multidecadal variability in precipitation simulated by state-of-the-art climate models, *Geophys. Res. Lett.*, 39, L21705, doi:10.1029/2012GL053424.

Ault, T. R., C. Deser, M. Newman, and J. Emile-Geay (2013), Characterizing decadal to centennial variability in the equatorial Pacific during the last millennium, *Geophys. Res. Lett.*, 40, 3450–3456, doi:10.1002/grl.50647.

Ba, J., et al. (2014), A multi-model comparison for Atlantic multidecadal variability, *Clim. Dyn.*, 9, 2333–2348.

Behera, S. K., and Y. Yamagata (2001), Subtropical SST dipole events in the southern Indian Ocean, *Geophys. Res. Lett.*, 28, 327–330, doi:10.1029/2000GL011451.

Beraki, A. F., D. G. DeWitt, W. A. Landman, and C. Olivier (2014), Dynamical seasonal climate prediction using an ocean-atmosphere coupled climate model developed in partnership between South Africa and the IRI, *J. Clim.*, 27, 1719–1741.

Brown, J. R., A. F. Moise, and A. Colman (2013), The South Pacific Convergence Zone in CMIP5 simulations of historical and future climate, *Clim. Dyn.*, 41, 2179–2197.

Carvalho, L. M. V., C. Jones, and B. Liebmann (2004), The South Atlantic Convergence Zone: Intensity, form, persistence, and relationship with intraseasonal to interannual activity and extreme rainfall, *J. Clim.*, 17, 88–108.

Clifford, P., S. Richardson, and D. Hemon (1989), Assessing the significance of the correlation between two spatial processes, *Biometrics*, 45, 123–134.

Colberg, F., and C. J. C. Reason (2007), Ocean model diagnosis of low-frequency climate variability in the South Atlantic region, *J. Clim.*, 20, 1016–1034.

Compo, G. P., J. S. Whitaker, and P. D. Sardeshmukh (2006), Feasibility of a 100 year reanalysis using only surface pressure data, *Bull. Am. Meteorol. Soc.*, 87, 175–190.

Compo, G. P., et al. (2011), The twentieth century reanalysis project, *Q. J. R. Meteorol. Soc.*, 137, 1–28.

Cook, K. H. (2000), The South Indian Convergence Zone and interannual rainfall variability over southern Africa, *J. Clim.*, 13, 3789–3804.

Cook, K. H. (2001), A Southern Hemisphere wave response to ENSO with implications for southern Africa precipitation, *J. Atmos. Sci.*, 15, 2146–2162.

Cook, K. H. (2004), Wet and dry spells within particularly wet and dry summers in the South African summer rainfall region, *Clim. Res.*, 26, 17–31.

Crétat, J., Y. Richard, B. Pohl, M. Rouault, C. J. C. Reason, and N. Fauchereau (2012), Recurrent daily rainfall patterns over South Africa and associated dynamics during the core of the austral summer, *Int. J. Climatol.*, 32, 261–273.

Czaja, A., P. van der Vaart, and J. Marshall (2002), A diagnostic study of the role of remote forcing in tropical Atlantic variability, *J. Clim.*, 15, 3280–3290.

Dieppois, B., M. Rouault, and M. New (2015), The impact of ENSO on southern African rainfall in CMIP5 ocean atmosphere coupled climate models, *Clim. Dyn.*, 45, 2425–2442.

Dutilleul, P. (1993), Modifying the *t* test for assessing correlation between two spatial processes, *Biometrics*, 49, 305–314.

Dyer, T. G. J., and P. D. Tyson (1977), Estimating above and below normal rainfall periods over South Africa, 1972–2000, *J. Appl. Meteorol.*, *16*, 145–147.

Enfield, D. B., and D. Mayer (1997), Tropical Atlantic sea surface temperature variability and its relation to El Niño–Southern Oscillation, *J. Geophys. Res.*, *102*, 929–945, doi:10.1029/96JC03296.

Farge, M. (1992), Wavelet transforms and their applications to turbulence, *Annu. Rev. Fluid Mech.*, *24*, 395–457.

Fauchereau, N., S. Trzaska, Y. Richard, P. Roucou, and P. Camberlin (2003), Sea-surface temperature co-variability in the southern Atlantic and Indian Oceans and its connections with the atmospheric circulation in the Southern Hemisphere, *Int. J. Clim.*, *23*, 663–677.

Fauchereau, N., B. Pohl, C. J. C. Reason, M. Rouault, and Y. Richard (2009), Recurrent daily OLR patterns in the southern Africa/southwest Indian Ocean region, implications for South African rainfall and teleconnections, *Clim. Dyn.*, *32*, 575–591.

Fogt, R. L., and D. H. Bromwich (2006), Decadal variability of the ENSO teleconnection to the high-latitude South Pacific governed by coupling with the Southern Annular Mode, *J. Clim.*, *19*, 979–997.

Folland, C. K., D. E. Parker, A. Colman, and R. Washington (1999), Large scale modes of ocean surface temperature since the late nineteenth century, in *Beyond El Niño: Decadal and Interdecadal Climate Variability*, vol. 4, edited by A. Navarra, pp. 73–102, Springer, Berlin.

Frankignoul, C., and E. Kestenare (2002), The surface heat flux feedback. Part I: Estimates from observations in the Atlantic and the North Pacific, *Clim. Dyn.*, *19*, 633–647.

Grinsted, A., J. C. Moore, and S. Jevrejva (2004), Application of the cross wavelet transform and wavelet coherence to geophysical time series, *Nonlinear Proc. Geophys.*, *11*, 561–566.

Hamed, K. H., and A. R. Rao (1998), A modified Mann-Kendall trend test for autocorrelated data, *J. Hydrol.*, *204*, 182–196.

Harris, I., P. D. Jones, T. J. Osborn, and D. H. Lister (2014), Updated high-resolution grids of monthly climatic observations—The CRU TS3.10 Dataset, *Int. J. Clim.*, *34*, 623–642.

Hart, N. C. G., C. J. C. Reason, and N. Fauchereau (2012a), Cloud bands over southern Africa: Seasonality, contribution to rainfall variability and modulation by the MJO, *Clim. Dyn.*, *41*, 119–1212.

Hart, N. C. G., C. J. C. Reason, and N. Fauchereau (2012b), Building a tropical extratropical cloud band metbot, *Mon. Weather Rev.*, *140*, 4005–4016.

Hashizume, H., S.-P. Xie, W. T. Liu, and K. Takeuchi (2001), Local and remote atmospheric response to tropical instability waves: A global view from the space, *J. Geophys. Res.*, *106*, 10,173–10,185, doi:10.1029/2000JD900684.

He, Y.-C., H. Drange, Y. Gao, and M. Bentsen (2016), Simulated Atlantic Meridional Overturning Circulation in the 20th century with an ocean model forced by reanalysis-based atmospheric data sets, *Ocean Model.*, *100*, 31–48.

Henley, B. J., J. Gergis, D. J. Karoly, S. Power, J. Kennedy, and C. K. Folland (2015), A tripole index for the Interdecadal Pacific Oscillation, *Clim. Dyn.*, doi:10.1007/s00382-015-2525-1, in press.

Hermes, J. C., and C. J. C. Reason (2005), Ocean model diagnosis of interannual coevolving SST variability in the South Indian and South Atlantic Oceans, *J. Clim.*, *18*, 2864–2882.

Hirahara, S., M. Ishii, and Y. Fukuda (2014), Centennial-scale sea surface temperature analysis and its uncertainty, *J. Clim.*, *27*, 57–75.

Hoell, A., C. Funk, T. Magadzire, J. Zinke, and G. Husak (2015), El Niño–Southern Oscillation diversity and southern Africa teleconnections during Austral Summer, *Clim. Dyn.*, *45*, 1583–1599.

Huang, B., V. F. Banzon, E. Freeman, J. Lawrimore, W. Liu, T. C. Peterson, T. M. Smith, P. W. Thorne, S. D. Woodruff, and H. M. Zhang (2015), Extended Reconstructed Sea Surface Temperature Version 4 (ERSST.v4). Part I: Upgrades and intercomparisons, *J. Clim.*, *28*, 911–930.

Johnson, N. C. (2013), How many ENSO flavors can we distinguish?, *J. Clim.*, *26*, 4816–4827.

Jury, M. K. (2014), Factors contributing to a decadal oscillation in South African rainfall, *Theor. Appl. Climatol.*, *120*, 227–237.

Kane, R. P. (2009), Periodicities, ENSO effects and trends of some South African rainfall series: An update, *S. Afr. J. Sci.*, *105*, 199–207.

Keenlyside, N. S., M. Latif, J. Jungclauss, L. Kornblueh, and E. Roeckner (2008), Advancing decadal-scale climate prediction in the North Atlantic sector, *Nature*, *453*, 84–88.

Kirtman, B., et al. (2013), Near-term climate change: Projections and predictability, in *Climate Change 2013: The Physical Science Basis. Contribution of Working Group I to Fifth Assessment Report of the Intergovernmental Panel on Climate Change*, edited by T. F. Stocker et al., pp. 953–1028, Cambridge Univ. Press, Cambridge, U. K., and New York.

Klein, S. A., B. J. Soden, and N. C. Lau (1999), Remote sea surface variations during ENSO: Evidence for a tropical atmospheric bridge, *J. Clim.*, *12*, 917–932.

Kruger, A. C. (1999), The influence of the decadal-scale variability of summer rainfall on the impact of El-Niño and La Niña events in South Africa, *Int. J. Clim.*, *19*, 59–68.

Latif, M., and T. P. Barnett (1994), Causes of decadal climate variability over the North Pacific and North America, *Science*, *266*, 634–637.

L'Heureux, M. L., and D. W. J. Thompson (2006), Observed relationships between the El Niño–Southern Oscillation and the extratropical zonal-mean circulation, *J. Clim.*, *19*, 276–287.

Lindesay, J. A. (1988), South African rainfall, the Southern Oscillation and a Southern Hemisphere semi-annual cycle, *J. Clim.*, *8*, 17–30.

Lübbecke, J. F., C. W. Böning, N. S. Keenlyside, and S.-P. Xie (2010), On the connection between Benguela and equatorial Atlantic Niños and the role of the South Atlantic Anticyclone, *J. Geophys. Res.*, *115*, C0915, doi:10.1029/2009JC005964.

Lyon, B., and S. J. Mason (2007), The 1997–98 summer season in southern Africa. Part I: Observations, *J. Clim.*, *20*, 5134–5148.

Macron, C., B. Pohl, Y. Richard, and M. Bessafi (2014), How do tropical-temperate troughs form and develop over southern Africa?, *J. Clim.*, *27*, 1633–1647.

Malherbe, J., F. A. Engelbrecht, W. A. Landman, and C. J. Engelbrecht (2012), Tropical systems from the southwest Indian Ocean making landfall over the Limpopo River Basin, southern Africa: A historical perspective, *Int. J. Climatol.*, *32*, 1018–1032.

Malherbe, J., W. A. Landman, and F. A. Engelbrecht (2014), The bi-decadal rainfall cycle, Southern Annular Mode and tropical cyclones over the Limpopo River Basin, southern Africa, *Clim. Dyn.*, *42*, 3121–3138.

Malherbe, J., B. Dieppois, P. Maluleke, M. Van Staden, and D. L. Pillay (2016), South African droughts and decadal variability, *Nat. Hazards*, *80*, 657–681.

Mantua, N. J., and S. R. Hare (2002), The Pacific Decadal Oscillation, *J. Oceanogr.*, *58*, 35–44.

Mantua, N. J., S. R. Hare, Y. Zhang, J. M. Wallace, and R. C. Francis (1997), A Pacific interdecadal climate oscillation with impacts on salmon production, *Bull. Am. Meteorol. Soc.*, *78*, 1069–1079.

Maraun, D. (2006), What can we learn from climate data? Methods for fluctuation time/scale and phase analysis, PhD thesis, Univ. of Postdam, Postdam, Germany.

Mason, S. J. (1990), Temporal variability of sea surface temperatures around southern Africa: A possible forcing mechanism for eighteen-year rainfall oscillation?, *S. Afr. J. Sci.*, *86*, 243–252.

Mason, S. J., and M. Jury (1997), Climatic variability and change over the southern Africa: A reflection on underlying processes, *Prog. Phys. Geogr.*, *21*, 23–50.

Menary, M. B., D. L. R. Hodson, J. I. Robson, R. T. Sutton, R. A. Wood, and J. A. Hunt (2015), Exploring the impact of CMIP5 model biases on the simulation of North Atlantic decadal variability, *Geophys. Res. Lett.*, *42*, 5926–5934, doi:10.1002/2015GL064360.

Mills, C. M., and J. E. Walsh (2013), Seasonal variation and spatial patterns of the atmospheric component of the Pacific Decadal Oscillation, *J. Clim.*, *26*, 1575–1594.

Minobe, S. (2000), Spatio-temporal structure of pentadecadal variability over the North Pacific, *Prog. Oceanogr.*, *47*, 381–408.

Morioka, Y., T. Tozuka, and T. Yamagata (2012), Subtropical dipole modes simulated in a coupled general circulation model, *J. Clim.*, *25*, 4029–4047.

Morioka, Y., T. Tozuka, and T. Yamagata (2013), How is the Indian Ocean subtropical dipole excited?, *Clim. Dyn.*, *41*, 1955–1968.

Morioka, Y., F. Engelbrecht, and S. Behera (2015), Potential sources of multidecadal climate variability over southern Africa, *J. Clim.*, doi:10.1175/JCLI-D-15-0201.01, in press.

Mulenga, H. M., M. Rouault, and C. J. C. Reason (2003), Dry summers over north-eastern South Africa and associated circulation anomalies, *Clim. Res.*, *25*, 29–41.

Nicholson, S. E. (1997), An analysis of the ENSO signal in the tropical Atlantic and western Indian Oceans, *Int. J. Clim.*, *17*, 345–375.

Nicholson, S. E., and J. Kim (1997), The relationship of the El Niño–Southern Oscillation to African rainfall, *Int. J. Clim.*, *17*, 117–135.

Nnamchi, H. C., J. Li, F. Kucharski, I.-S. Kang, P. Chang, and R. Farneti (2016), An equatorial-extratropical dipole structure of the Atlantic Niño, *J. Clim.*, doi:10.1175/JCLI-D-15-0894.1, in press.

Nonaka, M., and S.-P. Xie (2003), Covariations of sea surface temperature and wind over the Kuroshio and its extension: Evidence for ocean-to-atmosphere feedback, *J. Clim.*, *16*, 1404–1413.

Palmer, T. N., F. J. Doblas-Reyes, A. Weisheimer, and M. J. Rodwell (2008), Toward seamless prediction: Calibration of climate change projections using seasonal forecasts, *Bull. Am. Meteorol. Soc.*, *89*, 459–470.

Phillipon, N., M. Rouault, Y. Richard, and A. Favre (2012), The influence of ENSO on winter rainfall in South Africa, *Int. J. Clim.*, *32*, 2333–2347.

Pierce, D. W. (2002), The role of sea surface temperature in interactions between ENSO and the North Pacific Oscillation, *J. Clim.*, *15*, 1295–1308.

Poccard, I., S. Janicot, and P. Camberlin (2000), Comparison of rainfall structures between NCEP/NCAR reanalyses and observed data over tropical Africa, *Clim. Dyn.*, *16*, 897–915.

Pohl, B., N. Fauchereau, Y. Richard, M. Rouault, and C. J. C. Reason (2009), Interactions between synoptic, intraseasonal and interannual convective variability over southern Africa, *Clim. Dyn.*, *33*, 1033–1050.

Pohl, B., N. Fauchereau, C. J. C. Reason, and M. Rouault (2010), Relationships between the Antarctic Oscillation, the Madden-Julian Oscillation, and ENSO, and consequences for rainfall analyses, *J. Clim.*, *23*, 238–254.

Pohl, B., M. Rouault, and S. Sen Roy (2014), Simulation of the annual and diurnal cycles of rainfall over southern Africa by a regional climate model, *Clim. Dyn.*, *43*, 2207–2226.

Power, S., and R. Colman (2006), Multi-year predictability in a coupled general circulation model, *Clim. Dyn.*, *26*, 247–272.

Power, S., T. Casey, C. K. Folland, A. Colman, and V. Mehta (1999), Inter-decadal modulation of the impact of ENSO on Australia, *Clim. Dyn.*, *15*, 319–323.

Ratnam, J. V., S. K. Behera, Y. Masumoto, and T. Yamagata (2014), Remote effects of El Niño and Modoki events on the austral summer precipitation of southern Africa, *J. Clim.*, *27*, 3802–3815.

Rayner, N. A., D. E. Parker, E. B. Horton, C. K. Folland, L. V. Alexander, D. P. Rowell, E. C. Kent, and A. Kaplan (2003), Global analyses of sea surface temperature, sea ice, and night marine air temperature since the late nineteenth century, *J. Geophys. Res.*, *108*(D14), 4407, doi:10.1029/2002JD002670.

Reason, C. J. C. (2002), Sensitivity of the southern African circulation to dipole sea-surface temperature patterns in the South Indian Ocean, *Int. J. Clim.*, *22*, 377–393.

Reason, C. J. C., and D. Jagadheesha (2005), Relationships between South Atlantic SST variability and atmospheric circulation over the South African region during austral winter, *J. Clim.*, *18*, 3059–3075.

Reason, C. J. C., and M. Rouault (2002), ENSO-like decadal variability and South Africa rainfall, *Geophys. Res. Lett.*, *29*(13), 161–164, doi:10.1029/2002GL014663.

Reason, C. J. C., and M. Rouault (2005), Links between the Antartic Oscillation and winter rainfall over western South Africa, *Geophys. Res. Lett.*, *32*, L07705, doi:10.1029/2005GL022419.

Reason, C. J. C., M. Rouault, J. L. Melice, and D. Jagadeesha (2002), Interannual winter rainfall variability in SW South Africa, and large scale ocean-atmosphere interactions, *Meteor. Atmos. Phys.*, *80*, 19–29.

Reynolds, R. W., N. A. Rayner, T. M. Smith, D. C. Stokes, and W. Wang (2002), An improved in situ and satellite SST analysis for climate, *J. Clim.*, *15*, 1609–1625.

Richard, Y., N. Fauchereau, I. Poccard, M. Rouault, and S. Trzaska (2001), XXth century droughts in southern Africa: Spatial and temporal variability, teleconnections with oceanic and atmospheric conditions, *Int. J. Clim.*, *21*, 873–885.

Richard, Y., S. Trzaska, P. Roucou, and M. Rouault (2000), Modification of the southern African rainfall variability/El Niño–Southern Oscillation relationship, *Clim. Dyn.*, *16*, 883–895.

Ropelewski, C. F., and M. S. Halpert (1987), Global and regional scale precipitation patterns associated with the El Niño/Southern Oscillation, *Mon. Weather Rev.*, *115*, 1606–1626.

Ropelewski, C. F., and M. S. Halpert (1989), Precipitation patterns associated with the high indices phase of the Southern Oscillation, *J. Clim.*, *2*, 268–284.

Rouault, M. (2012), Bi-annual intrusion of tropical water in the northern Benguela upwelling, *Geophys. Res. Lett.*, *39*, L12606, doi:10.1029/2012GL052099.

Rouault, M., and Y. Richard (2005), Intensity and spatial extent of droughts in southern Africa, *Geophys. Res. Lett.*, *32*, L15702, doi:10.1029/2005GL022436.

Sang, Y. F. (2013), A review on the applications of wavelet transform in hydrological time series analysis, *Atmos. Res.*, *122*, 8–15.

Schaefli, B., D. Maraun, and M. Holschneider (2007), What drives flow events in the Swiss Alps? Recent developments in wavelet spectral analysis and their application to hydrology, *Adv. Water Resour.*, *30*, 2511–2525.

Schneider, N., and B. D. Cornuelle (2005), The forcing of the Pacific Decadal Oscillation, *J. Clim.*, *18*, 4355–4373.

Schneider, U., A. Becker, P. Finger, A. Meyer-Christoffer, M. Ziese, and B. Rudolf (2014), GPCC's new land surface precipitation climatology based on quality controlled in situ data and its role in quantifying the global water cycle, *Theor. Appl. Climatol.*, *115*, 15–40.

Seager, R., N. Harnik, Y. Kushnir, W. Robinson, and J. Miller (2003), Mechanisms of hemispherically symmetric variability, *J. Clim.*, *16*, 2960–2978.

Suzuki, R., S. K. Behera, S. Iizuka, and T. Yamagata (2004), The Indian Ocean subtropical dipole simulated using a CGCM, *J. Geophys. Res.*, *109*, C09001, doi:10.1029/2003JC001974.

Taguchi, B., H. Nakamura, M. Nonaka, N. Komori, A. Kuwano-Yoshida, K. Takaya, and A. Goto (2012), Seasonal evolutions of atmospheric response to decadal SST anomalies in the North Pacific subarctic frontal zone: Observations and a coupled model simulation, *J. Clim.*, *25*, 111–139.

Tanimoto, Y., H. Nakamura, T. Kagimoto, and S. Yamane (2003), An active role of extratropical sea surface temperature anomalies in determining anomalous turbulent heat flux, *J. Geophys. Res.*, *108*(c10), 3304, doi:10.1029/2002JC001750.

Taylor, K. E., R. J. Stouffler, and G. A. Meehl (2012), An overview of CMIP5 and the experiment design, *Bull. Am. Meteorol. Soc.*, *93*, 485–498.

Thompson, D. W. J., and J. M. Wallace (2000), Annular modes in the extratropical circulation. Part I: Month-to-month variability, *J. Clim.*, *13*, 1000–1016.

Todd, M. C., and R. Washington (1999), Circulation anomalies associated with tropical-temperate troughs in southern Africa and the southwest Indian Ocean, *Clim. Dyn.*, *15*, 937–951.

Todd, M. C., R. Washington, and P. I. Palmer (2004), Water vapour transport associated with tropical-temperate trough systems over southern Africa and the southwest Indian Ocean, *Int. J. Clim.*, *24*, 555–568.

Toniazzo, T. (2009), Climate variability in the south-eastern Pacific and its relation with ENSO: A GCM study, *Clim. Dyn.*, *34*, 1093–1114.

Torrence, C., and G. P. Compo (1998), A practical guide to wavelet analysis, *Bull. Am. Meteorol. Soc.*, *79*, 61–78.

Torrence, C., and P. Webster (1999), Interdecadal changes in the ENSO-monsoon system, *J. Clim.*, *12*, 679–690.

Tourre, Y. M., and W. B. White (1995), ENSO signals in global upper-ocean temperature, *J. Phys. Oceanogr.*, *25*, 1317–1332.

Tourre, Y. M., B. Rajagopalan, Y. Kushnir, M. Barlow, and W. B. White (2001), Patterns of coherent ocean decadal and interdecadal climate signals in the Pacific basin during the 20th century, *Geophys. Res. Lett.*, *28*, 2069–2072, doi:10.1029/2000GL012780.

Tourre, Y. M., C. Cibot, L. Terray, W. B. White, and B. Dewitte (2005) Quasi-decadal and inter-decadal climate fluctuations in the Pacific Ocean from a CGCM, *Geophys. Res. Lett.*, *32*, L07710, doi:10.1029/2004GL022087.

Tourre, Y. M., Y. Kushnir, and W. B. White (1999), Evolution of interdecadal variability in sea level pressure, sea surface temperature, and upper ocean temperature over the Pacific Ocean, *J. Phys. Oceanogr.*, *9*, 1528–1541.

Tyson, P. D. (1981), Atmospheric circulation variations and the occurrence of extended wet and dry spells over southern Africa, *J. Clim.*, *1*, 115–130.

Tyson, P. D. (1986), *Climatic Change and Variability Over Southern Africa*, Oxford Univ. Press, Cape Town.

Vecchi, G. A., S.-P. Xie, and A. S. Fischer (2004), Ocean-atmosphere covariability in the western Arabian Sea, *J. Clim.*, *17*, 1213–1224.

Venegas, S., L. A. Mysak, and D. N. Straub (1997), Atmosphere-ocean coupled variability in the South Atlantic, *J. Clim.*, *10*, 2904–2920.

Vigaud, N., Y. Richard, M. Rouault, and N. Fauchereau (2009), Moisture transport between the South Atlantic Ocean and southern Africa: Relationships with summer rainfall and associated dynamics, *Clim. Dyn.*, *32*, 113–123.

Vizy, E. K., and K. H. Cook (2016), Understanding long-term (1982-2013) multi-decadal change in the equatorial and subtropical South Atlantic climate, *Clim. Dyn.*, *46*, 2087–2113.

Wallace, J. M., T. P. Mitchell, and C. Deser (1989), The influence of sea surface temperature on surface wind in the eastern equatorial Pacific: Seasonal and interannual variability, *J. Clim.*, *2*, 1492–1499.

Wang, S., J. Huang, Y. He, and Y. Guan (2014), Combined effects of the Pacific Decadal Oscillation and El Niño–Southern Oscillation on global land dry-wet changes, *Sci. Rep.*, *4*, 6651, doi:10.1038/srep06651.

Washington, R., and A. Preston (2006), Extreme wet years over southern Africa: Role of Indian Ocean sea surface temperatures, *J. Geophys. Res.*, *111*, D15104, doi:10.1029/2005JD006724.

Wu, Z., N. E. Huang, S. R. Long, and C.-K. Peng (2007), On the trend, detrending, and variability of nonlinear and nonstationary time series, *Proc. Natl. Acad. Sci. U.S.A.*, *104*, 14,889–14,894.

Xie, S. P. (2004), Satellite observations of cool ocean-atmosphere interaction, *Bull. Am. Meteorol. Soc.*, *85*, 195–208.

Yue, S., and C. Wang (2004), The Mann-Kendall test modified by effective sample size to detect trend in serially correlated hydrological series, *Water Resour. Manag.*, *18*, 201–218.

Zhang, G. J., and M. J. McPhaden (1995), The relationship between sea surface temperature and latent heat flux in the equatorial Pacific, *J. Clim.*, *8*, 589–605.

Zhang, Y., J. M. Wallace, and D. S. Battisti (1997), ENSO-like interdecadal variability: 1900–93, *J. Clim.*, *10*, 1004–1020.